JCI The Journal of Clinical Investigation

TP53/TAU axis regulates microtubule bundling to control alveolar stem cell mediated regeneration

Satoshi Konishi, Khaliun Enkhbayar, Shuyu Liu, Naoya Miyashita, Yoshihiko Kobayashi, Vera Hutchison, Ashna Sai, Pankaj Agarwal, Jonathan Witonsky, Nathan D. Jackson, Max A. Seibold, Jichao Chen, Aleksandra Tata, Purushothama Rao Tata

J Clin Invest. 2026. https://doi.org/10.1172/JCI194762.

Research In-Press Preview **Cell biology** **Pulmonology**

Graphical abstract

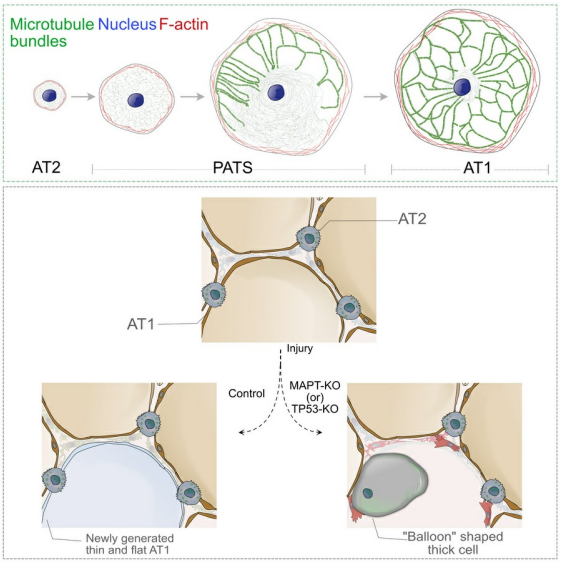

Find the latest version:

https://jci.me/194762/pdf

TP53/TAU axis regulates microtubule bundling to control alveolar stem cell mediated regeneration

Satoshi Konishi[1#], Khaliun Enkhbayar[1,2#], Shuyu Liu[1], Naoya Miyashita[1], Yoshihiko Kobayashi[1,13], Vera Hutchison[3], Ashna Sai[1], Pankaj Agarwal[1], Jonathan Witonsky[4], Nathan D. Jackson[5], Max A. Seibold[5, 6 7], Jichao Chen[3,8], Aleksandra Tata[1,2,9,*], Purushothama Rao Tata[1,9,10,11,12,14*]

[1] Department of Cell Biology, Duke University School of Medicine, Durham, NC, 27710, USA

[2] Department of Surgery, Surgical Sciences, Duke University School of Medicine, Durham, NC, 27710, USA

[3] Department of Pulmonary Medicine, University of Texas MD Anderson Cancer Center, Houston, Texas 77030, USA

[4] Department of Pediatrics, University of California, San Francisco, 550 16th Street, San Francisco, CA 94158, USA

[5] Center for Genes, Environment and Health, National Jewish Health, Denver, CO, USA

[6] Department of Pediatrics, National Jewish Health, Denver, CO, USA

[7] Division of Pulmonary Sciences and Critical Care Medicine, University of Colorado School of Medicine; Aurora, CO, USA.

[8] Department of Pediatrics, Perinatal Institute Division of Pulmonary Biology, University of Cincinnati and Cincinnati Children's Hospital Medical Center, Cincinnati, OH, 45229, USA.

[9] Duke Regeneration Center, Duke University, Durham, NC, 27710, USA

[10] Division of Pulmonary, Allergy, and Critical Care Medicine, Department of Medicine, Duke University School of Medicine, Durham, NC, 27710, USA

[11] Center for Advanced Genomic Technologies, Duke University, Durham, NC, 27710, USA

[12] Duke Cancer Institute, Duke University School of Medicine, Durham, NC, 27710, USA

[13] Present address: Medical Research Laboratory, Institute of Integrated Research, Institute of Science Tokyo, Bunkyo-ku, Tokyo, 113-8510, Japan

[14] Lead contact

# denotes co-first authors

*Corresponding authors. Address correspondence to: Purushothama Rao Tata, 303 Research Drive, Sands Building Room 451, Durham, NC, 27710, USA. Phone: 919-684-0624. Email: purushothamarao.tata@duke.edu and Aleksandra Tata, 303 Research Drive, Sands Building Room 448, Durham, NC, 27710, USA. Phone: 919-684-0624. Email: aleksandra.tata@duke.edu.

Declaration of interests

The authors have declared that no conflict of interest exists.

Abstract

Cells exhibit diverse sizes and shapes, tailored for functional needs of tissues. Lung alveoli are lined by large, extremely thin epithelial alveolar type-1 cells (AT1s). Their characteristic morphology is essential for lung function and must be restored after injury. The mechanisms underlying small, cuboidal alveolar type-2 cells (AT2s) differentiation into thin AT1s remain elusive. Here, we demonstrated that AT2s undergo a stepwise morphological transformation characterized by the development of a unique thick microtubule (MT) bundle organization, critical for AT1 morphology. Using AT2 cultures and *in vivo* genetic loss of function models, we found that MT bundling process occurs in a transitional cell state during AT2 differentiation and was regulated by the TP53/TAU signaling axis. Notably, TAU underwent a linear clustering process, forming beads-on-a-string-like pattern that preceded thick MT-bundle formation. Genetic gain or loss of function of TAU in mouse or human models, prevented the formation of thick MT-bundles, highlighting the critical role of precise TAU levels in generating ultra-thin AT1s. This defect was associated with increased tissue fibrosis following bleomycin-induced injury *in vivo*. GWAS analysis revealed risk variants in MAPT locus in lung diseases. Moreover, TP53 controlled TAU expression and its loss phenocopied TAU deficiency. This work revealed an unexpected role for TAU in organizing MT-bundles during AT2 differentiation.

Introduction

Tissues must maintain proper cellular composition and morphological organization to carry out their functions. Defects in either cellular composition or structure have been implicated in various diseases such as cancers, organ fibrosis and tissue atrophy (1–4). Therefore, it is essential to understand the mechanisms that allow cells to achieve their appropriate identity and often

complex cell morphology during development, homeostasis, and repair. In the lung, the gas-exchanging alveoli have an extremely thin epithelial lining that both facilitates diffusion of gases and serves as a barrier (5). About 95% of this lining is occupied by AT1s, one of the thinnest cell types in the human body (6–9). The remaining area is occupied by the apical domains of small cuboidal AT2s, which serve as facultative stem cells that can self-renew and differentiate into AT1s both at homeostasis and after injury.

Multiple growth factor signaling and transcriptional regulators have been implicated in AT2-to-AT1 differentiation during development and regeneration (10–25). Additionally, cells must coordinate structural components such as actin, microtubules, and cytokeratin to provide a cytoskeleton to build and support the cell body. Indeed, recent studies have implicated actin-dependent biophysical forces mediated by breathing movements and CDC42 mechanical stretch in the maintenance of AT1 identity or AT2-to-AT1 differentiation, respectively(18, 26). Additionally, integrins and cytokeratins have been shown to play critical roles in AT2-to-AT1 differentiation via regulation of immune cell-mediated alveolar epithelial repair processes(27, 28). Previous studies have demonstrated that AT2-to-AT1 differentiation involves a transitional state (also known as PATS, DATPs or KRT8hi-ADIs), which the abnormal induction or persistence of can induce fibrotic responses in alveolar fibroblasts leading to pulmonary fibrosis (29–33). Nevertheless, the relationship between programs that drive PATS and those that effect morphological changes remain elusive. Specifically, little is known about the transcriptional programs that guide structural components to shape the thin, expansive morphology of AT1s.

Here, we show that AT2-to-AT1 differentiation is associated with a MT bundling process that is essential for them to acquire large and thin morphology. Specifically, using a newly optimized 2-dimensional culture model, we have uncovered a dynamic process in which individual radial MTs are remodeled to generate thick MT-bundles. This process is mediated by TAU (encoded by the Microtubule-Associated Protein Tau (*MAPT*) gene), which is highly expressed in PATS and AT1s

and localized to thick MT-bundles. Genetic gain and loss of function of TAU leads to disorganization of MTs, loss of thick MT-bundles, and disruption in AT1 generation both *ex vivo* and *in vivo*. Furthermore, we show that loss of function of the transcription factor TP53 regulates TAU and recapitulates phenotypes observed in TAU mutant cells.

Results

Newly optimized conditions for AT2 maintenance and differentiation in 2-dimensional cultures

To assess morphological dynamics during mouse AT2-to-AT1 differentiation, we sought to optimize 2-dimensional cultures that enable efficient cell state transitions. Previous studies have demonstrated that AT2s can be cultured in 50% matrigel (10, 34). To establish a 2D-culture model, AT2s were first plated on 5% Matrigel coated wells. However, even at later times both large and thin cells that express AGER (AT1 marker) and ABCA3 (AT2 marker) were observed, suggesting incomplete differentiation (Supplemental Figure 1A). On Collagen-I coated plates tightly packed colonies of cells expressing ABCA3 and SFTPC were present throughout the culture duration (Supplemental Figure 1B). By contrast, culture on fibronectin coated plates revealed the presence of $CLDN4^{+}$ PATS and large and thin $AGER^{+}$ AT1-like cells at early (day-5) and later (day-9) times (Figure 1A and Supplemental Figure 1C). To visualize the morphological dynamics during AT2-to-AT1 differentiation, we performed time-lapse live imaging of cells cultured on fibronectin starting day-3 for 72 hours. Our data revealed gradual stretching of AT1-like cells with the appearance of arborizing cytoskeletal components from day-6 that were maintained throughout the culture duration (Supplemental Figure 1D and Video S1). We then performed bulk RNA sequencing (RNA-seq) on cells collected from collagen-1 (AT2s) and fibronectin coated plates harvested on day-5 (PATS) and day-9 (AT1s) (Figure 1A). As expected, differential gene expression analysis revealed previously reported AT2 (*Sftpa1, Abca3, Sftpc, Lamp3*), PATS (*Krt8, Sfn, Sox4*), and AT1 (*Hopx, Aqp5, Ager, Cav1*) markers in different culture

conditions (Supplemental Figure 1E). Together, we established a 2-dimensional culture system to maintain AT2s and their differentiation to AT1s in defined conditions.

Transcriptome profiling revealed dynamic expression pattern of structural and regulatory components of microtubules during AT2-to-AT1 differentiation

Our above live imaging data revealed the appearance of arborizing cytoskeletal structures. To further evaluate these structures, we analyzed the above transcriptome data and found expression of transcripts related to both structural (*Tuba1c, Tuba1b, Tuba1a*) and regulatory (*Map6, Mapre3, Map1a, Map2, Kif1a, Camsap1*) components of MT assembly in specific cell types. We found enrichment of multiple structural and regulatory components of MTs in PATS and AT1s indicating that MTs undergo significant reorganization during AT2 differentiation to AT1 via PATS (Figure 1B). To assess whether such changes occur during AT2 differentiation *in vivo*, we reevaluated previously generated scRNA-seq data from bleomycin-induced lung injury(30). We found enrichment of *Tubb2b, Tubb5, Tubb6, Map1b, Map4,* and *Map7* in PATS, whereas *Tuba1a, Tuba8, Tubb2a, Tubb4b, Map2*, and *Map6* were enriched in AT1s (Supplemental Figure 2A). Together, transcriptome data revealed dynamic expression of MT components during AT2 to AT1 differentiation both *in vivo* and *ex vivo*.

MTs undergo dynamic reorganization and generate thick bundles during AT2-toAT1 differentiation ex vivo and in vivo

We next performed immunostaining to visualize expression and localization of MTs, actin and cytokeratins during AT2 to AT1 differentiation. AT2s have a dense network of individual radial MT-fibers distributed throughout the cell body. By contrast, AT1s have organized thick bundle-like structures each composed of multiple individual MT-fibers (Figure 1C and Supplemental Figure 2B). Interestingly, MT changes correlate with an increase in cell area and decrease in cell thickness (Figure 1D). Immunostaining for TUBA1B revealed a dynamic change in its localization

as AT2s differentiate to AT1s via PATS. On day-5, we observed the emergence of individual thick MT-bundles, whereas on day-9, cells had a highly branched network of thick bundles all around the cell body as the cells mature to AT1s (Figure 1C). In most cell types, MTs are anchored to the peri-nuclear Golgi via microtubule organizing centers (MTOCs) (35, 36). To assess Golgi localization, we performed immunostaining for GM130 (37). Golgi apparatus is restricted to peri-nuclear regions in PATS. Whereas it is co-localized with thick MT-bundles including at branch points in AT1s, suggesting that the Golgi serves as an anchoring point for MTs, as in neuronal axons (38, 39) (Figure 1E). Additionally, staining for PK-mito, LAMP1 and CANX, which marks mitochondria, lysosomes and ER, respectively, revealed that these organelles co-localize with thick MT-bundles (Supplemental Figure 2C). Furthermore, immunostaining for acetylated tubulin (Ac-TUB), a marker of stabilized form of MTs, revealed that thick MT-bundles correlate with mature forms of MTs (40) (Figure 1F). Of note, immunostaining for TUBA1A, TUBA1B, and MAP2 showed thick MT-bundles are composed of multiple tubulin classes and MT-associated proteins (MAPs) (Figure 1F and Supplemental Figure 2D). Among the actin and intermediate filaments, KRT8 localization overlapped with tubulins within the thick MT-bundles whereas actin (phalloidin) is highly enriched in the cortex and the basal side of the cells (Figure 1C, G and Supplemental Figure 2E).

To assess whether the thick MT-bundles observed in 2D cultures are also present in AT1s *in vivo,* we utilized the *Rtkn2-CreER;R26R-Kaleidoscope* (hereafter referred as *Rtkn2-Kaleidoscope*) mouse line, which expresses TUBA1C fused to green fluorescent protein (EGFP) (41). Administration of tamoxifen (*in vivo*) or adeno-cre virus (*ex vivo*) activates the expression of TUBA1C-EGFP, thereby enabling the localization of tubulins specifically in AT1s (Figure 1H). To assess TUBA1C-EGFP protein localization in cultured cells, we purified AT2s from *Rtkn2-Kaleidoscope* mice and cultured them as described above (Figure 1H). As expected, we found radial distribution of TUBA1C-EGFP throughout the cell body in AT2s from Kaleidoscope mice

whereas AT1s exhibited EGFP localization in a pattern similar to that of thick MT-bundles (Figure 1I and Supplemental Figure 2F). To assess the tubulin localization pattern *in vivo*, lungs were collected from tamoxifen administered *Rtkn2-Kaleidoscope* mice followed by thick tissue sectioning and imaging to visualize large, flat and thin AT1s in alveolar sacs. Confocal imaging followed by maximum intensity projection revealed EGFP localization consistent with AT1s having thick MT-bundles *in vivo* (Figure 1I).

MTs are polar structures with a fast growing plus end and a slow growing minus end that collectively provide the directionality of MT growth (42). We utilized end-binding 1 (EB1)-EGFP that allows tracking of MT plus ends to assess MT growth directionality and kinetics in real-time. 2D-cultured mouse AT2s were transduced with lentiviral *EB1-EGFP* followed by live imaging at early (day-7) and late stages (day-14) of differentiation to capture these dynamics in PATS and AT1s, respectively (Figure 1J and Video S2 and S3). Time-lapse imaging and comet tracking revealed that cells at day-7 showed unidirectional movement from center to cortex, whereas cells from day-14 showed bidirectional growth. This finding was further confirmed by kymograph-based quantification analysis (Figure 1K and Video S2 and S3). These data suggest that alveolar epithelial cells shift their MT growth from unidirectional to bidirectional as the AT2s differentiate into large and thin AT1s. Moreover, an increase in EB1 comet velocity and angle fluctuation on day-14, indicated enhanced MT dynamics and polymerization and switching directions within bundled tracks (Figure 1L). Additionally, a decrease in directionality concentration, and track straightness at day-14 compared to day-7 suggested that emergence of bidirectional movement along bundled MTs during PATS-to-AT1 transition (Figure 1L). Together, AT2-PATS-AT1 differentiation processes can be recapitulated in our 2D *ex vivo* culture system revealing a unique thick MT-bundle organization pattern in AT1s.

Dynamic expression and localization of TAU during AT2 differentiation

The above data revealed that MT components and associated genes are differentially expressed during AT2 to AT1 differentiation. Among these, MAPs are known to directly bind MTs and facilitate their nucleation in neurons and oligodendrocytes (43). To evaluate the expression of MAPs, we plotted relative expression of relevant genes in a pseudotime trajectory encompassing AT2, PATS, and AT1s using time-series scRNA-seq data that captured cellular dynamics at different times following bleomycin-induced lung injury (30). Unexpectedly, we found that *Mapt* (encoding TAU), a gene that has been extensively studied in Parkinson's and Alzheimer's diseases, is dynamically expressed during AT2-to-AT1 differentiation (44, 45). Specifically, *Mapt* expression is gradually increased as AT2s transition to PATS with highest expression in AT1s (Figure 2A). Furthermore, this expression pattern correlated with that of MT components including *Tuba1b*, suggesting that TAU plays a role in assembling MTs. To validate its expression in AT1s *in vivo*, we performed co-immunostaining for TAU and AGER on thick tissue sections followed by imaging and maximum intensity projection (Figure 2B). To further evaluate its expression and localization dynamics, we carried out co-immunostaining for TAU and TUBA1B on cells collected at different times during AT2-to-AT1 differentiation. In line with transcriptome data, we found a gradual increase in TAU levels as AT2s differentiate into AT1s via PATS (Figure 2C and Supplemental Figure 3A). Although it is expressed at low levels in AT2s, TAU shows a punctate localization pattern throughout the cell body. Notably, the localization changed to an organized fiber-like pattern as AT2s transition to PATS. Super resolution imaging revealed that multiple TAU puncta are organized into beads-on-a-string like pattern in PATS and in mature AT1s (Supplemental Figure 3B). Interestingly, the fiber-like pattern resembled that of thick MT-bundle pattern even in the absence of clear bundles of TUBA1B, suggesting that TAU-fibers precede MT-bundle formation. At later times, dense thick MT-bundles are formed in mature AT1s. These data suggest a model in which TAU is organized into a string like pattern that precedes thick MT-bundle formation during AT2-to-AT1 differentiation(Figure 2D).

Loss or gain of TAU disrupts thick MT-bundle formation and AT1 cell thickness ex vivo

To assess the role of TAU during AT2 differentiation, we performed CRISPR-based *Mapt* knockout in purified AT2s in culture. First, we screened for efficient gRNAs selected from a previously described mouse Brie genome-wide gRNA library (46). Of the four gRNAs screened, two gave knockout efficiencies of 97% (gRNA 1) and 67% (gRNA 4) as assessed by ICE analysis (47) (Supplemental Figure 4A and B). Then we generated adeno-associated viral 2/6 (AAV6) particles expressing gRNAs and GFP followed by transduction into AT2s purified from *H11-Cas9* mice and harvested cells for analysis on day-9 post infection (48). AAV6 co-expressing non-targeting control (NTC) gRNA and GFP served as a control. Co-immunostaining for TAU and GFP (infected cells) revealed efficient deletion of the gene in *Mapt* gRNA infected cells but not in controls (Figure 3A and B; Supplemental Figure 4C and D). As expected, *Mapt* gRNA infected GFP^+ cells lacked thick MT-bundles compared to NTC gRNA infected cells. Immunostaining for GFP and TUBA1B and Ac-TUB revealed disorganized MTs dispersed throughout the cell body in *Mapt* gRNA1 infected cells, further validating the above observations (Figure 3C and D). Quantification revealed a significant decrease in the number of cells with thick MT-bundles in *Mapt* gRNA1 cells compared to NTC gRNA. Furthermore, we found a significant increase in the apical-basal thickness of *Mapt* gRNA1 versus NTC gRNA infected cells (Figure 3E). We observed similar phenotypes using *Mapt* gRNA4 (Supplemental Figure 4E).

Previous studies using *in vitro* reconstitution assays revealed that a fine balance in the levels of TAU is essential for its proper assembly, localization and MT organization (49, 50) To assess whether an increase in TAU levels affects MT-bundle formation during AT2-to-AT1 differentiation, we ectopically expressed TAU in AT2s. Full length *Mapt* coding sequence from mouse fused with FLAG-tag was used to generate AAV6-mouse *Mapt-Flag* vectors. Similarly, human full length *MAPT* was cloned into a plasmid expressing GFP and was used to generate AAV6-human *MAPT-GFP* virus. AAV6-GFP served as a control (Figure 3F). Co-immunostaining for GFP/FLAG, TAU, TUBA1B, Ac-TUB, and TUBA1A revealed disorganized MTs in both mouse

and human TAU gain of function conditions compared to controls (Figure 3G, H and Supplemental Figure 5A). Quantification further revealed a significant loss of thick MT-bundles in MAPT gain of function cells compared to controls. Additionally, *Mapt* gain of function cells showed a significant decrease in cell area and increase in cell thickness, a phenotype similar to that seen in *Mapt* loss of function (Figure 3A-I). In certain brain tauopathies, a mutation in TAU at amino acid position 301 with proline to lysine substitution is known to have gain of function activity and to disrupt MT organization (51–53). Therefore, we ectopically expressed a pathological form of TAU (TAU^{P301L}) co-expressing GFP in mouse AT2s during their differentiation. Immunostaining for TUBA1B, TAU, GFP, TUBA1A, and Ac-TUB revealed disorganization of tubulins and lack of thick MT-bundles in GFP^{+} cells (Supplemental Figure 5B). Further, to assess whether MT-bundles are essential for maintaining AT1 cell thickness, we deleted or ectopically expressed *Mapt* once MT-bundles were established in cultured AT1s. To do so, we first generated AT1s followed by delivery of *Mapt*-gRNA or *mMapt*-OE on day-9, at which point the AT1s established MT-bundles. Immunostaining for Ac-TUB and quantification of MT-bundles on day-6 post gRNA delivery revealed that *Mapt*-gRNA and *Mapt*-OE transduced cells lacked MT-bundles (Supplemental Figure 5C, D). Strikingly, we found a significant increase in cell thickness in *Mapt*-gRNA and OE cells compared to controls (Supplemental Figure 5E). Collectively, these data suggest that both loss and gain of TAU function alters MT-bundle formation, and AT1 cellular organization.

TAU is required for proper organization of cells during AT2-to-AT1 differentiation in vivo

Next, we sought to study the role of TAU *in vivo* utilizing a previously described constitutive *Mapt* deletion (*Mapt-KO*) mouse model (54) and assessing AT2-to-AT1 differentiation after bleomycin-induced lung injury. To assess the morphology of cells derived from AT2s, we specifically labeled AT2s with GFP using AAV5-GFP virus in control and *Mapt-KO* mice prior to bleomycin administration (55). This approach also allowed us to identify regions undergoing repair in response to bleomycin-induced injury (Supplemental Figure 6A). Co-immunostaining for GFP and

AGER on thick tissue sections revealed large, flat and thin AGER$^+$ AT1s derived from GFP$^+$ AT2s in control lungs. As expected, confocal single stack shows that GFP labeled AT1s in control lungs exhibit a thin cell morphology. In contrast, *Mapt-KO* lungs showed thick and balloon-shaped GFP$^+$ cells that extrude into the alveolar lumina and lack AT1 markers (Supplemental Figure 6B). Further assessment revealed a significant decrease in the number of thin cells (0-6μm) and an increase in thick cells (13-40μm) in *Mapt-KO* compared to controls (Supplemental Figure 6C).

To exclude the possibility of non-cell autonomous effects in the above experiments, we performed CRISPR based loss of *Mapt* function specifically in AT2s. For this, we generated AAV5 virus carrying *Mapt* or NTC gRNAs and a green fluorescent protein (GFP marks infected cells) and administered them intranasally into *H11-Cas9* mouse lungs prior to bleomycin-induced injury (Figure 4A). As expected, co-immunostaining for GFP and AGER followed by imaging of thick tissue sections revealed large, thin, and flat cells co-expressing these markers in NTC gRNA lungs. However, *Mapt* gRNA transduced cells showed a thick and balloon-shaped morphology and protruded into alveolar lumina (Figure 4B). Quantification further revealed a significant decrease in the number of thin cells (0-6μm) and an increase in thick cells (13-40μm) in *Mapt* gRNA administered lungs compared to controls (Figure 4C). Collectively, these data suggest that loss of *Mapt* leads to defects in cell organization *in vivo.*

Previous studies revealed that defects in AT2-to-AT1 differentiation exacerbates alveolar fibrosis after bleomycin-induced injury. Therefore, we sought to assess the consequences of loss of TAU on alveolar repair and fibrosis (Figure 4A). Co-immunostaining for GFP with ACTA2 and TAGLN revealed an increase in myofibroblasts in *Mapt* gRNA administered lungs compared to NTC lungs (Figure 4D and 4E). Moreover, quantification revealed a significant increase in ACTA2-expressing regions in areas that have GFP expression, suggesting that defective repair leads to an increase in fibrosis in these lungs compared to controls (Figure 4F). Additionally, immunostaining and

quantification for SFN (early PATS) and LGALS3 (late PATS) on sections collected from bleomycin injured control and *Mapt* gRNA administered lungs revealed a significant increase in SFN^+ and decrease in $LGALS3^+$ PATS in *Mapt*-depleted cells (Figure 4G and 4H). These data suggest an impairment in alveolar epithelial differentiation in *Mapt*-deleted cells. Furthermore, trichome staining revealed an increase in collagen deposition in bleomycin injured *Mapt*-deleted lungs compared to controls (Figure 4I). Analysis of bleomycin injured *Mapt-KO* mice further confirmed these findings (Supplemental Figure 6D-H). Together, these data demonstrate that TAU regulates MT dynamics during AT2 differentiation that is required to ensure AT1 regeneration after injury.

Loss of TP53 disrupts TAU expression, MT and AT1 organization during AT2-AT1 differentiation

In neurons from Alzheimer's disease and in certain carcinomas, TP53 and TAU directly interact to control cellular processes such as DNA damage repair and cellular stress pathways (56). Previous studies have also implicated a role for TP53 in AT2 to AT1 differentiation after injury (17, 29, 30). To assess the role of TP53 in regulation of TAU and MT assembly, we purified AT2s from *Sftpc-creER;R26-tdT;Trp53$^{f/f}$* (here after referred as *Trp53-KO*) mice that had received tamoxifen. AT2s from C57Bl6 mice served as controls (Figure 5A). Using our 2D cultures, we assessed the ability of AT2s to differentiate into AT1s, as well as MT organization and TAU expression. Immunostaining and western blot analysis revealed that TAU expression is decreased in *Trp53-KO* cells compared to controls (Figure 5B and Figure 5C). Moreover, localization pattern of TUBA1B and TUBA1A correlated with disorganization of MTs including the loss of thick MT-bundles in *Trp53-KO* cells (Figure 5B). Additionally, immunostaining revealed a decrease in expression of AGER in mutant cells compared to controls (Figure 5B). Of note, mutant cells exhibited more than 2 nuclei, a finding consistent with previous reports that suggested a role for TP53 in regulating gamma-tubulin and blocking cytokinesis (57, 58). Consistent with MT disorganization, mutant cells showed an increase in cell thickness and a slight decrease in cell

area compared to controls (Figure 5B). To assess MT dynamics, we transduced a lentivirus carrying EB1-GFP fusion protein into AT2s lacking TP53 (Figure 5D). Time-lapse imaging and comet tracking analyses and velocity, directionality, and angle fluctuation quantification revealed that cells at day-7 showed premature bidirectional movement of MTs from center to cortex, which was maintained at day-14, suggesting that they undergo misdirected growth in mutant cells (Figure 1K, 1L, 5E, 5F and Video S4 and S5).

To assess the consequences of TP53 deficiency on alveolar epithelial organization, we utilized *Sftpc-tdT-Trp53-KO* mice. Upon tamoxifen administration, there is concomitant expression of tdTomato and loss of *Trp53* specifically in AT2s. *Sftpc-creER;R26-tdT* (hereafter referred as *Sftpc-tdT*) mice served as a control (Figure 5G). To assess the consequences of TP53 loss on alveolar epithelial cell organization, we administered bleomycin to cause lung injury and collected tissues on day-13 post injury (Figure 5G). Co-immunostaining for AGER and tdTomato on thick tissue slices followed by confocal 3D reconstruction of alveoli revealed large and thin cells co-expressing tdTomato and AGER in control lungs. In contrast, we observed large balloon-shaped tdTomato expressing cells that lacked AGER in TP53 deficient cells, a phenotype similar to that of TAU mutant cells (Figure 4B and 5H). Quantification further confirmed a significant increase in cell thickness in TP53 deficient cells compared to controls (Figure 5I). To assess whether TP53 directly binds on *Mapt* genomic locus, we reanalyzed a previously described ChIP-seq data from purified PATS (29). Integrative Genomics Viewer (IGV) tracks revealed enrichment of TP53 on *Mapt* promoter (Figure 5J). Additionally, we found TP53 binding on multiple tubulin and MT-associated gene loci (Figure 5K and Supplemental Figure 7A). To further test whether the expression of tubulin and microtubule-associated genes is altered in TP53 deficient cells, we utilized previously published scRNA-seq data (17). Pseudo-bulk RNA expression analysis of this data revealed that the expression of *Map1b, Map2, Map4, Map6, Map7, Tuba1b, Tuba1c, Tubb4b, Tubb5, and Tubb6* was decreased in *Trp53* knock-out cells (Figure Supplemental Figure

7B). Additionally, to assess whether TP53 similarly controls tubulin and MAP encoding genes in human cells, we reanalyzed a publicly available scRNA-seq data from lung adenocarcinoma (59). Although these datasets lack TP53 mutation annotation, the majority of tumor cells exhibit decreased *TP53* transcript levels (consistent with loss-of-function or nonsense mutations). We found that *MAP2, MAP4, MAP7, TUBA1A, TUBB4B, TUBB6*, and *TUBG2*, were downregulated in TP53-low cells (Figure Supplemental Figure 7C). Together, these data point to a mechanism whereby TP53 directly binds and controls tubulin and MAP encoding genes during AT2 to AT1 differentiation.

TAU expression, localization, and requirement during human AT2 differentiation

We then sought to assess TAU expression, localization and requirement during human AT2 differentiation. First, we purified human AT2s as previously described and cultured them in serum-free, feeder free (SFFF) conditions for expansion or in alveolar differentiation medium (ADM) for differentiation into AT1s on plates coated with either collagen or FN as described above (Figure 1A, Supplemental Figure1A-C, and 6A). As expected, these culture conditions supported either selective expansion of AT2s or their differentiation into large, thin, and flat AT1s *ex vivo* as assessed by co-immunostaining for SFTPC and HTI-56, respectively, (Figure 6B). Furthermore, immunostaining for TUBA1B revealed the presence of thick MT-bundles in the AT1s. We then assessed the expression and localization dynamics of TAU at early and late stages in culture. Co-immunostaining for TAU, TUBA1B, TUBA1A, and Ac-TUB revealed a gradual increase in TAU expression as the AT2s differentiate to AT1s. Further, TAU localization changed from random puncta to an organized fiber-like pattern that aligned along the thick MT-bundles similar to results seen in mice (Figure 6C).

Second, to test the requirement of TAU for proper differentiation of AT2s into AT1s, we screened and selected a gRNA that can efficiently target human *MAPT* gene (Supplemental

Figure 8A). As illustrated in Figure 6D, we generated lenti-viral particles expressing Cas9, *MAPT* gRNA, and a fluorescent reporter, mCherry, and transduced them into human AT2s. NTC gRNA served as a control. Transduced cells were then induced to differentiate into AT1s and collected on day-9 post infection for analysis. Co-immunostaining for mCherry, TAU, and Ac-TUB revealed loss of TAU and absence of thick MT-bundles in *MAPT* gRNA transduced cells compared to NTC gRNA (Figure 6E). Further, we found disorganization of morphology from thin, large, and flat in the case of NTC gRNA transduced cells to thick and elongated in *MAPT* gRNA transduced cells. To assess the consequences of TAU gain of function, we transduced AAV6 expressing human *MAPT* and GFP into AT2s. Of note, ectopic expression of TAU in AT2s was not sufficient to induce AT2-AT1 differentiation (Supplemental Figure 8B). However, induction of differentiation by administering ADM resulted in the disorganization of cell morphology specifically in ectopic TAU expressed cells compared to controls as revealed by co-immunostaining for GFP, TAU, and Ac-TUB (Figure 6F). Additionally, ectopic TAU expressing cells showed abnormal thick MT-bundles. Together, both gain and loss of TAU disrupted MT organization and gave rise to thick cells during human AT2 to AT1 differentiation, similar to what had been observed with mouse cells.

Genetically regulated MAPT expression within the 17q21.31 haplotype influences pulmonary disease risk

Common genetic variation at the *MAPT*-containing 17q21.31 locus has been strongly associated with IPF, COPD, and lung function traits (60–64). More specifically, this locus includes a 900kb inversion, which contains genetic variation in strong linkage disequilibrium, resulting in the H1 and H2 inversion-tagging haplotypes (65). Consequently, these pulmonary disease associations reflect haplotype-level association, rather than a single SNP. Within, the disease-associated haplotype, we found no *MAPT* nonsynonymous coding variants. Rather most haplotype variants localized to the *MAPT* locus are non-coding, consistent with the idea that if disease risk is conferred by this locus, it is through *MAPT*-expression regulation. To explore this, we examined

MAPT eQTL data from nasal airway epithelial brushings generated on a childhood asthma cohort (GALA=681). *MAPT* was identified as a significant nasal eGene, with genetic variation tagging the inversion haplotype associated with *MAPT*-expression (Supplemental Figure 8C). Examining *MAPT*-expression by one of the eQTL variants, rs1981997, we found that the minor allele (A) was associated with lower *MAPT*-expression (Supplemental Figure 8D). Notably, the A allele of rs1981997 has been associated with decreased IPF risk (60). In contrast, based on data reported by the GTEx consortium in lung tissue, the A allele for rs1981997 is associated with increased *MAPT*-expression. GTEx also reports rs1981997 as a *MAPT* eQTL across 18 additional tissues, with the direction of effect sometimes matching that of lung tissue and other times matching the nasal pattern. Together, these results support a model whereby genetically regulated *MAPT*-expression within the 17q21.31 haplotype influences pulmonary disease risk, with the direction of effect depending on the tissue context.

Discussion

Efficient diffusion of gases across the alveolar epithelium into the blood capillaries and vice versa requires that these tissues maintain appropriate cell numbers and organization (6, 66). Here, we describe a unique MT organization, in which differentiating AT1s develop thick MT-bundles that control cell thickness and area. We speculate that such thick MT-bundle organization promotes the expansion of the cytoplasm and decrease in cell thickness that enhances gas diffusion as compared to the radial and dispersed pattern observed in AT2s and other cell types. Furthermore, thick MT-bundles likely provide structural support and stability for the thin and expansive AT1s during cyclic breathing movements. Our work uncovered an unexpected role for TAU in alveolar epithelial differentiation. Specifically, TAU seems to undergo condensation and is organized into a beads-on-a-string like pattern in PATS and in AT1s. We also find that TAU localization precedes thick MT-bundle formation suggesting that TAU initiates MT organization during AT2 differentiation. This aligns with prior studies using *in vitro* reconstitution assays that revealed TAU

droplet formation and localized condensation, which in turn facilitates MT assembly (50). Further, it has been shown that TAU is critical for assembly of well-organized MTs and spacing between bundles in neuronal axons and dendrites (67, 68). Previous studies have implicated that endothelium derived TAU promotes neuronal tauopathy in *Pseudomonas aeruginosa* infected mice (69, 70). However, to our knowledge, this is the first report implicating TAU in alveolar epithelial stem cell mediated repair after injury.

Our data revealed that both gain and loss of TAU disrupted thick MT-bundle formation leading to generation of aberrant differentiated cells with an increase in cell thickness and decrease in cell area. These data suggest that a fine balance in the expression levels of TAU is essential to control thick MT-bundle formation and cellular organization. In tauopathies, it has been well documented that hyper-phosphorylation and different splice forms of TAU can differently influence MT organization, organelle transport and mitochondrial function (71). Future studies need to evaluate the role of these different isoforms in alveolar epithelial cells. Interestingly, AT1s share some similarities with oligodendrocytes. For instance, oligodendrocytes generate elaborate myelin sheaths that wrap around neuronal axons, facilitating rapid signal conduction. Both cell types express *Mapt* and generate expansive membrane, which in turn is regulated by MTs and MAPs (72–76). Additionally, both AT1s and oligodendrocytes express the transcription factor MYRF (myelin regulatory factor). Based on this, we propose that both AT1s and oligodendrocytes use similar programs to generate expansive membranes via TAU and organized MT structures.

Our study also revealed that expression of TAU is decreased upon loss of transcription factor TP53 during AT2 differentiation. Aside from its well-known functions in genome stability, DNA damage repair and cell death pathways, previous studies have also implicated a role for TP53 in regulating cytoskeleton in alveolar epithelial cells (29). We now implicate a role for TP53 in regulating TAU expression and thereby MT organization during differentiation of alveolar epithelial cells. This is in line with previous studies that revealed a role for TP53 in directly

regulating the expression of MAPs in neurons and other cells (56). Indeed, we find that loss of TP53 leads to altered MT-bundle formation, generation of aberrant alveolar epithelial cells with an increase in cell thickness, a phenotype similar to TAU loss of function. These data suggest that TP53/TAU axis controls thick MT-bundle formation to control cellular alveolar epithelial cell organization.

Recent genome-wide association studies have identified potential risk variants in the *MAPT* locus in COPD and pulmonary fibrosis patients (60, 61). In addition to *MAPT*, this 17q21 locus also harbors other genes including *KANSL1,* which has been identified as a risk allele in eQTL studies that utilized scRNA-seq and GWAS data to compute risk allele association (77). Our analyses further provide support that variants in *MAPT* locus are associated with IPF disease risk. Together, these data indicate the need to further investigate the TAU association in IPF and COPD.

Material and Methods

Sex as a biological variable

Our study examined male and female animals, and similar findings are reported for both sexes.

Mouse strains, bleomycin injury and viral delivery

Both male and female mice aged between 8–16 weeks were used for experiments. All the mice were C57BL/6 unless otherwise indicated. The following mice were used for experiments: wild type, *Sftpc*$^{tm1(cre/ERT2)Blh}$ (*Sftpc-CreER*)(78), *B6.Cg-Gt(ROSA)26Sor*$^{tm14(CAG-tdTomato)Hze}$*/J* (*R26R-tdTomato*)(79), *H11-Cas9*(48), *Rtkn2-CreER;R26R-Kaleidoscope*(41) , *B6.129X1-Mapttm1Hnd/J* (54) and *Trp53*$^{fl/fl}$ (80) (mixed background). For lineage tracing mice received 3–5 doses of 2mg tamoxifen (Sigma-Aldrich) per 20g of body weight via intraperitoneal injection. For bleomycin-

induced lung injury, 2.5 U kg^{-1} bleomycin was administered intranasally 2 weeks after tamoxifen injection and the mice were monitored daily. Mice that were administered PBS served as controls. The mice were sacrificed at different times after bleomycin injury. For intranasal AAV viral infection, mice were anesthetized with 3% isoflurane in an induction chamber followed by 2.5e10 viral particles administration resuspended in 60µL of physiological saline (Henry Schein, 002477).

Mouse lung tissue dissociation and AT2 cell isolation

Lung dissociation was performed as described previously(34, 81). Briefly, lungs were inflated with an enzymatic dissociation solution (450U/mL *Collagenase I* (Worthington, LS004197), 5U/mL *Dispase* (Corning, 354235), and 0.33U/mL *DNase I* (Roche, 10104159001). Lung lobes were minced and incubated in enzyme solution at 37°C for 25–35min. Dissociation was quenched with 10% FBS/DMEM and strained. Cell pellet was resuspended in red blood cell lysis buffer (100µM EDTA, 10mM KHCO3, 155mM NH4Cl) for 2min, followed by quenching with 10% FBS/DMEM and filtration. For FACS sorting, the cell pellet was resuspended in a sorting buffer (0.5% BSA (Genclone, 25-529F), 2mM EDTA). Cells were stained with EpCAM/CD326-Brilliant-Violet-711 (Biolegend, 118233, 1:200), Lysotracker-Green DND-26 (Invitrogen, L7526, 1:10000), CD140a-PE (Biolegend, 135905, 1:200), CD31-eFluor-450 (Invitrogen, 48-0311-82, 1:200) and CD45-eFluor-450 (Invitrogen, 48-0451-82, 1:200). $EpCAM^{+}Lysotracker^{high}$ cells were collected in 2% FBS/DMEM/F12. Sorting was performed using either a SONY SH800S or MA900.

Collagen I, fibronectin and 5% Matrigel coating

To maintain AT2s collagen was used. Briefly, 100µl of Cellmatrix Type I-A (Wako Chemicals, 637-00653) was mixed with 100µl of DMEM-F12/Ham media and 20µl of reconstitution buffer (2.2g NaHCO3 in 100 ml of 0.05 N NaOH and 200 mM HEPES) was added. Ice-cold collagen solution was added to well, spread and polymerized at 37°C for 30min. AT2s were plated on collagen-coated wells. To induce mouse AT1 differentiation, AT2s were seeded on fibronectin. At

first, fibronectin (Millipore-sigma, F4759) was diluted with PBS to a concentration of 50µg/ml, added to wells at 37°C for 30min-6h. Fibronectin was removed, and wells were washed once with PBS followed by mouse AT2 seeding diluted in culture medium. For 2D-cultures on Matrigel, AT2s were plated on wells collated with 5% Matrigel (Corning, 354230). Briefly, Matrigel was serially diluted in DMEM/F12 to concentration of 5%, followed by well-coating at 37°C for 30min. Next, Matrigel was removed and AT2s were seeded. AT2s were cultured in SFFF medium. The medium was changed every two days.

Mouse AT2 cell expansion

Mouse AT2 organoids were cultured in SFFF conditions as described previously (34, 81). Briefly, 3000-5000 FACS-sorted AT2s were resuspended in SFFF media and mixed with Matrigel in droplet format. After Matrigel solidification at 37°C for 15-20min, the mouse SFFF medium was added. AT2 organoids were passaged to single cells using TrypLE select (Gibco, 12563029) every 10-12 days.

Human lung dissociation and AT2s purification

Human lung dissociation was performed as described previously (34, 81). Briefly, 2-3g of tissue was washed with PBS/1% Antibiotic-Antimycotic followed by pleura, small airway and vasculature removal. Remaining tissue was cut into small pieces followed by digestion (Collagenase type-I: 1.68mg/ml, Dispase: 5U/ml, DNase: 10U/ml) at 37°C for 1-1.5h. Cells were filtered and rinsed with 10% FBS/DMEM. Cell suspension was spun down at 450g for 10min and pellet was resuspended in red blood cell lysis buffer (Thermo Fisher Scientific, A1049201) for 5min, washed with 10% FBS/DMEM, filtered and pelleted. Approximately 2-10 million cells were resuspended in MACS (magnetic activated cell-sorting) buffer (PBS, 1% BSA, 2mM EDTA) as per manufacturer's instructions and incubated with TruStain-FcX (Biolegend, 422032) for 15min at 4ºC followed by mouse HTII-280 (1:60 dilution) antibody for 1h at 4ºC. Cells were washed twice

with MACS buffer and incubated with anti-mouse IgM microbeads for 15min at 4ºC, loaded into the LS-column (Miltenyi Biotec, 130-042-401) and collected magnetically.

Human AT2 cell culture and cell differentiation

Human AT2 cultures were performed as previously described (34, 81). Human AT2 organoids were cultured in SFFF conditions in 50% Matrigel. For differentiation, AT2s were dissociated and plated in 5% Matrigel and cultured in SFFF media for 3-5 days followed by 7-8 days of ADM media replacement containing 10% human serum.

EB1-EGFP lentivirus transduction

Lentivirus production was performed as described previously with modification (82). Briefly, 70-80% confluent HEK293T were prepared in 10% FBS/DMEM/1% penicillin-streptomycin. Two hours before transfection, the medium was changed to 5% FBS/DMEM without penicillin-streptomycin followed by transfection with 10μg of pLenti-EB1-EGFP (Addgene, plasmid 118084), 7μg psPAX2 (Addgene, plasmid 12260), and 5μg pCMV-VSV-G (Addgene, plasmid 8454) plasmids using PEI Max (1:4) (Polysciences, 24765). After overnight incubation, the medium was changed to 10% FBS/DMEM/1% penicillin–streptomycin. Viral supernatant was collected 48, 72, and 96h after transfection followed by virus concentration using Lenti-X Concentrator (Takara, 631231). The viral pellet was dissolved in DMEM/F12 and titrated using a qPCR lentivirus titter kit (Applied Biological Materials, LV900). Single cell suspensions of mouse AT2s were resuspended in SFFF containing lentivirus at 1:100 and seeded on fibronectin-coated glass bottom dish (Matsunami Glass, D35-14-1-U). Cells were incubated with lentivirus overnight followed by SFFF replacement.

Live cell imaging of EB1-EGFP signal in mouse AT2s and kymograph analysis

Virus infected mouse AT2s were recorded on days 7 and 14 at 1.5-second intervals. For kymograph analysis, the time series stack data was applied to the Fiji plugin software: *tubeness* to remove background signals followed by *KymoResliceWide* analysis according to the distributor's guide. Analysis including velocity, directionality concentration, angle fluctuation and track straightness were performed. Briefly, images were converted to 8-bit. A region of interest (ROI) was manually defined within the cell boundary. To enhance linear comet signals, the *tubeness* filter was applied. Tracking of EB1-comets was performed using the TrackMate plugin (Simple LAP tracker). All quantitative analyses were performed in R (packages: tidyverse, readr, ggplot2, circular). For each EB1-comet track, the XY displacement and duration were used to calculate velocity (μm/min) and movement angle (degrees). Directionality concentration (DC) was calculated using circular statistics to quantify the uniformity of comet movement angles, with higher DC values indicating more coherent orientation. Angle fluctuation was calculated as the standard deviation of frame-to-frame directional changes, reflecting local instability. Track straightness, defined as the ratio of net displacement to total path length, was quantified to evaluate the linearity of EB1-comet trajectories. All measurements were calibrated using the imaging scale (μm/pixel) and frame interval (s/frame).

Vector cloning of AAV-CRISPR KO plasmids

Candidate gRNA sequences were picked up from Brie library(46) or designed using CHOPCHOP(83). Two oligos containing sgRNA sequences (Oligo1:ACC+5'gRNA(20-mer)3', Oligo 2:AAC+5'Reverse complement of gRNA(20-mer)3') were obtained and annealed using T4PNK (NEB M0201S) according to the manufacturing protocol. Backbone plasmid: pAAV-U6-sgRNA-CMV-GFP (addgene:85451) was cut with restriction enzyme Sap1 (NEB, R0569S), and a larger size of cut-plasmid was extracted from gel. Finally, annealed oligo was ligated to backbone plasmid using Quick ligase (NEB, M2200S).

AAV production and transduction

AAV production and transduction was performed as previously described(55). Briefly, 70-80% confluent HEK293T cells were prepared in 10% FBS/DMEM/1% penicillin-streptomycin. Two hours before transfection, medium was changed to 5% FBS/DMEM without penicillin-streptomycin and cells were transfected using PEI Max (1:4) with 50μg of transgene plasmid, 100μg of adenovirus helper plasmid (XX680), and 50μg of AAV serotype plasmid. Following overnight incubation, the medium was replaced to 5% FBS/DMEM/1% penicillin–streptomycin. Viral supernatant was collected 4-days after transfection and purified by iodixanol gradient using Opti-prep Density Gradient Medium (Sigma, D1556) and ultracentrifuge. Titters of virus were measured by qPCR with primers amplifying the AAV2 ITR regions (fw:5′AACATGCTACGCAGAGAGGGAGTGG-3′; rev:5′-CATGAGACAAGGAACCCCTAGTGATGGAG-3′). For AAV transgene transduction to *ex vivo* culture, AAV supernatant was diluted with SFFF medium at a ratio of 1:4 to 1:5 without concentration and administered to cells.

RNA preparation and bulk RNA-seq

For total RNA extraction, cells were resuspended in TRIzol (Thermo Fisher Scientific, 15596026) and total RNA was extracted using Direct-zol RNA Microprep kit (Zymo, R2061) according to the manufacturer's protocol. Bulk RNAseq was conducted on samples with RIN values greater than 8.0 using a bioanalyzer. Ribosomal RNA from total RNA samples (100μg) was performed using NEBNext rRNA Depletion Kitv2 (NEB, E7400L). Libraries were prepared using NEBNext Ultra II Directional RNA Library Prep Kit for Illumina (NEB, 7760S).

Reanalysis of scRNA-seq data

Line plots of relative gene expression were performed by re-analyzing the available data (GSE 141259)(30). We extracted gene expression trajectory data from the converging trajectories using the interactive web tool (https://theislab.github.io/LungInjuryRegeneration/).

Bulk RNA sequencing and differential gene expression analysis

Purified RNA (1μg) from each sample was enriched for Poly-A RNA using NEBNext Poly(A) mRNA Magnetic Isolation Module (NEB, #E7490). Libraries were prepared using NEBNext Ultra II RNA Library Prep Kit for Illumina (NEB, #E7770). Paired-end sequencing (150bp for each read) was performed using HiSeq X with at least 15 million reads per sample. Quality of sequenced reads were assessed using FastQC (https://www.bioinformatics.babraham.ac.uk/projects/fastqc/). PolyA/T tails were trimmed using Cutadapt(84). Adaptor sequences were trimmed and reads shorter than 24bp were trimmed using Trimmomatic(85). Normalization and extraction of differentially expressed genes (DEGs) between samples were performed using an R package, DESeq2(86).

ChIP–seq Signal Filtering and Visualization

To visualize TP53 binding enrichment across microtubule-related genes, published ChIP–seq data for TP53 (GSE141635; $CTGF^{+}tdTomato^{+}$ PATS) and its corresponding Input control were processed using R (v4.3.2). Signal tracks in bedGraph format were imported via the rtracklayer package and converted into BigWig files after filtering by signal intensity and genomic coordinates for each gene were obtained from TxDb.Mmusculus.UCSC.mm10.knownGene and org.Mm.eg.db. ChIP and Input signals overlapping each gene region were extracted using subset ByOverlaps. Peaks with signal intensity greater than 5.29 were selected corresponding to the 95th percentile of the Input signal distribution. Only peaks exceeding this percentile were considered TP53-enriched relative to the Input control. The resulting BigWig files were loaded

into the Integrative Genomics Viewer (IGV) (v2.17.0) to visualize TP53 ChIP enrichment relative to Input across the analyzed microtubule-related genes.

Re-analysis of human and mouse scRNA-seq datasets to assess TP53-dependent regulation of AT1-associated microtubule gene programs

Re-analysis of publicly available scRNA-seq datasets (human lung adenocarcinoma (GSE131907)(59) and a Kras-driven mouse lung cancer model (GSE231681) (17) were conducted in Seurat v5.0.1. Briefly, for the human dataset, raw UMI matrices and cell annotations were filtered. Data were normalized, highly variable genes were selected, and PCA was performed. Cell-type annotations from the original study were incorporated as metadata, and AT1s were extracted. Malignant epithelial cells were stratified based on TP53 expression, and those with TP53 expression below the median were defined as TP53-low malignant. For the mouse dataset, raw HDF5 matrices were imported and filtered. Samples representing KT (*Trp53* WT), KPT (*Trp53* loss), and KFT (*Trp53* hyperactive) were merged and normalized, and the top 2,000 variable genes were identified. Scaled data were subjected to PCA, and principal components 1–30 were used for UMAP embedding and clustering. Cluster identities were assigned using canonical markers. AGER-positive AT1-like cells were extracted for analyses. KFT samples were excluded from KT–KPT comparisons. MAP and tubulin isoform genes were analyzed, and violin plots were generated.

GWAS data analyses

MAPT eQTL data based on nasal brushings were obtained from a published genome-wide GALA nasal eQTL analysis(87). The *MAPT* LocusZoom plot was constructed using the locuszoomr R package (88), where LD patterns were generated relative to the lead variant using LDlinkR based on the 1000 Genomes Project European population(89). Publicly available eQTL data were examined using the GTEx version 10 portal (gtexportal.org).

Lung tissue fixation and sectioning

Mouse lungs were inflated and fixed in 4% Paraformaldehyde (PFA) at 4°C for 4-6 hours. Lung lobes were separated and washed in PBS followed by incubation in 30% sucrose overnight at 4°C. Lobes were incubated in 1:1 30% sucrose:OCT for 1h followed by embedding in OCT blocks and cryosectioning at 8-10µm thickness.

Immunostaining on lung sections

OCT sections were washed with PBS. Antigen retrieval was performed using 10mM sodium citrate buffer at 90-95°C for 15min. Sections were washed with PBS, permeabilized in PBST (0.1% Triton X-100 in PBS), and incubated with 1% BSA in PBST for 30min at RT followed by primary antibodies at 4°C overnight. Sections were then washed 3x in PBST, incubated with secondary antibodies in blocking buffer for 1h at RT, washed with PBST 3x, and mounted using Fluor G with DAPI.

Immunostaining of cultured cells

Cultured cells were fixed with 4% PFA at RT for 15min or with methanol at -20°C for 10min. Samples were washed with PBS, permeabilized in 0.2% Triton X-100 in PBS, and incubated with 1% BSA in PBS for 30min at RT, followed by primary antibodies at 4°C overnight. Samples were then washed 3x in PBST, incubated with secondary antibodies for 1h at RT, washed with PBST 3x, and mounted.

Precision cut lung slices (PCLS) and immunostaining of PCLS

Mouse lungs were inflated with 2% low-melting agarose dissolved in PBS as previously described(90). PCLS (300µm) were obtained using compresstome (PRECISIONARY, VF510-Z). For immunostaining, PCLS were fixed in 4% PFA at 4°C for 1h. Sections were washed with PBS,

permeabilized in 0.3% Triton X-100 in PBS, and incubated with blocking buffer (1% BSA, 0.3% Triton X-100 in PBS) for 1h at RT followed by primary antibodies at 4°C overnight. Sections were then washed 3x in wash buffer (0.5% Tween-20, 0.5% Triton X-100 in PBS), incubated with secondary antibodies in blocking buffer at 4°C overnight, washed 3x in wash buffer and twice in PBS before imaging on glass bottom dish. Three-dimensional rendering of acquired stack images was performed using Imaris (Oxford instruments) or Icy software.

Protein extraction and western blot analysis

Cultured cells were washed with ice-cold PBS and collected in cell lysis buffer (50mM Tris-HCl, pH 7.5, 150mM NaCl, 1% Triton X-100, 2mM EDTA and 2mM DTT and protease inhibitor cocktail). Following a 15-minute incubation on ice, the lysates were spun down at 13,000g for 15min and the supernatant was collected for a Bradford analyses. Samples were prepared in Laemmli buffer, boiled for 10min at 95°C and loaded on 12% SDS-PAGE gels followed by transfer, blocking in 5% milk for 1h at RT, incubation with primary antibodies overnight at 4°C, washes with TBST and incubation with secondary antibodies. The following primary and secondary antibodies were used: anti-Tau (10274-1-AP, Proteintech, 1:1000), anti-GAPDH (GT239, GeneTex, 1:10000), anti-Rabbit IgG-HRP (4030-05, Southern Biotech, 1:10000), anti-Mouse IgG-HRP (1030-05, Southern Biotech, 1:10000). Signals were detected using a Pierce ECL-2. Band intensities were quantified using ImageJ.

Imaging of mitochondria and tubulin in mouse AT1s

Cultured AT1s were incubated for 30min at 37°C in SFFF media containing Tubulin Tracker Green (T34075, Invitrogen, 1:4000) and PKmito Orange Dye (CY-SC053, Cytoskeleton-Inc., 1:5000) followed by a 5min wash in SFFF containing 1µg/mL Hoechst-33342 stain. Cells were rinsed 3x in SFFF media and imaged.

Masson-Trichrome staining

Trichrome staining was performed using a Masson Trichrome Staining Kit (HT15-1KT, Sigma-Aldrich) and a Weigert's Iron Hematoxylin Set (HT1079-1SET, Sigma-Aldrich) according to manufacturer protocols on OCT-frozen sections. Images were recorded using a 20X objective of Axio imager (Zeiss).

Antibodies

The following antibodies and dyes were applied to samples for immunostaining: anti-RAGE/AGER (MAB1179, R&D systems, 1:500), anti-proSP-C (AB3786, MilliporeSigma, 1:500), anti-ABCA3 (3C9) (sc58220, Santacruz, 1:300), anti-Claudin4 (36-4800, Invitrogen, 1:200), anti-Actin, alpha-Smooth Muscle Cy3-conjugated (C6198, MilliporeSigma,1:500), anti-HT1-56 (TB-29AHT1-56, Terrace Biotech, 1:300), anti-HTII-280 (TB-27AHT2-280, Terrace Biotech, 1:50), anti-GFP (NB100-1770, Novus Biologicals, 1:500), anti-tdTomato (AB8181-200, Origene, 1:1000), anti-TUBA1A antibody (PA5-22060, Invitrogen, 1:100), anti-TUBA1B (66031-1-Ig, Proteintech, 1:500), anti-acetylated Tubulin (66200-1-Ig, Proteintech, 1:500), anti-Tau (10274-1-AP, Proteintech, 1:200), anti-Tau-1 (PC1C6) (MAB3420, MilliporeSigma,1:100), anti-Tau (Tau-5) (AHB0042, Invitrogen,1:50), anti-MAP2 (17490-1-AP, Proteintech, 1:500), anti-Keratin8 (TROMA-I, DSHB, 1:50), anti-GM130 (610822, BD, 1:50), Alexa Fluor-555 Phalloidin (A34055, Invitrogen,, 1:400), Alexa Fluor-647 Phalloidin (A22287, Invitrogen,, 1:400), LEL-DyLight®-649 (DL-1178, Vector Laboratories,1:1500), anti-FLAG-M2 (F1804, Sigma-Aldrich, 1;1000), anti-Calnexin (AB22595, Abcam, 1:500), anti-CD107a/LAMP-1 (121601, BioLegend, 1:500), anti-SFN (PA5-95056, Invitrogen, 1:250), anti-LGALS3-Alexa647 (125408, BioLegend, 1:500), anti-TAGLN/Transgelin (ab14106, Abcam, 1:250).

Image acquisition, processing and quantification

Images were captured using an Olympus FV3000 confocal microscope with a 20X, 30X, 40X, 60X objectives. For long term live-imaging Olympus VivaView FL Incubator Microscope was used with 20x objective. Images were processed using the Olympus CellSens application or ImageJ and Figures were prepared using Affinity Designer. Measurements and quantifications were performed using Image J-Fiji using a sample of biological replicates (n=3).

Statistical analysis

Statistical methods relevant to each Figure are outlined in the Figure legend. Sample size was not predetermined. Data are presented as means with standard error (SEM). Statistical analysis was performed in Excel, Prism and R. A two-tailed Student's t-test was used for the comparison between two experimental conditions. We used Shapiro-Wilk analyses to test whether data are normally distributed and used Mann-Whitney statistical test for the comparison between two conditions that showed non-normal distributions.

Study approval

The animal experiments were approved by the Duke University Institutional Animal Care and Use Committee in accordance with US National Institutes of Health guidelines. Healthy human lungs were obtained in accordance with Institutional Review Board oversight (Duke University Pro00114526– exempt research as described in 45 CFR 46.102(f), 21 CFR 56.102(e) and 21 CFR 812.3(p) which satisfies the Privacy Rule as described in 45CFR164.514).

Data Availability Statement

All quantification values represented in the graphs are provided in the Supporting Date Values file. Requests for further information and resources should be directed to and will be fulfilled by Purushothama Rao Tata (purushothamarao.tata@duke.edu). Bulk RNA-seq data of cultured cells have been deposited at GEO (GSE287523) and are publicly available as of the date of publication.

Acknowledgements

We thank Brigid Hogan and Tata lab members for fruitful discussions, Lauren Macadlo and Viet Dung Nguyen for technical support and the Duke Compute Cluster for server space and data storage. We acknowledge and thank the BioRepository and Precision Pathology Center (BRPC) and Research Support (SSCRS)-Duke Surgery for providing human tissues under Institutional Review Board oversight and Substrate Services Core. The authors thank the participants and their families for their contribution, and the health care professionals and clinics for their support and participation in the Genes-Environments and Admixture in Latino Americans Study. Flow Cytometry was performed in the Duke Cancer Institute Flow Cytometry Facility at Duke University.

Funding support

This work is the result of NIH funding, in whole or in part, and is subject to the NIH Public Access Policy. Through acceptance of this federal funding, the NIH has been given a right to make the work publicly available in PubMed Central. Flow Cytometry is supported by the NCI Cancer Center Support Grant (P30CA014236). S.K and Y.K. were supported by the Japan Society for the Promotion of Science Overseas Research Fellowships. This work was supported by research award from NHLBI/NIH (R01HL146557, R01HL160939, R01HL153375 to P.R.T and R01HL174525 to A.T).

Author contributions

S.K. and K.E. were designated co-first authors as S.K. led the initial study design, experiments, and manuscript draft, K.E. led the major revision, including key experimental design, execution, and analysis. S.L performed experiments and analyzed data. N.M., Y.K., and P.A. performed transcriptome data analysis. A.S. assisted in immunostaining experiments. V.H and J.C. provided lungs from *Rtkn2-CreER;R26R-Kaleidoscope* mice. M.A.S, J.W., and N.D.J. performed GWAS

analyses. A.T. co-designed and supervised the work, performed image acquisition, co-wrote the manuscript, and prepared Figures. P.R.T. conceived, co-designed, and supervised the work and co-wrote the manuscript. All authors reviewed and edited the manuscript.

References:

1. Henderson NC, Rieder F, Wynn TA. Fibrosis: from mechanisms to medicines. *Nature*. 2020;587(7835):555–566.

2. Watt FM, Jordan PW, O'Neill CH. Cell shape controls terminal differentiation of human epidermal keratinocytes. *Proc Natl Acad Sci U S A*. 1988;85(15):5576–5580.

3. Miroshnikova YA, et al. Adhesion forces and cortical tension couple cell proliferation and differentiation to drive epidermal stratification. *Nat Cell Biol*. 2018;20(1):69–80.

4. Luxenburg C, Zaidel-Bar R. From cell shape to cell fate via the cytoskeleton - Insights from the epidermis. *Exp Cell Res*. 2019;378(2):232–237.

5. Weibel ER. Morphological basis of alveolar-capillary gas exchange. *Physiological Reviews*. 1973;53(2):419–495.

6. Crapo JD, et al. Cell number and cell characteristics of the normal human lung. *Am Rev Respir Dis*. 1982;125(6):740–745.

7. Hogan BLM, et al. Repair and regeneration of the respiratory system: complexity, plasticity, and mechanisms of lung stem cell function. *Cell Stem Cell*. 2014;15(2):123–138.

803 8. Basil MC, et al. The Cellular and Physiological Basis for Lung Repair and Regeneration: Past,
804 Present, and Future. *Cell Stem Cell*. 2020;26(4):482–502.

805 9. Konkimalla A, Tata A, Tata PR. Lung Regeneration: Cells, Models, and Mechanisms. *Cold*
806 *Spring Harb Perspect Biol*. 2021;a040873.

807 10. Barkauskas CE, et al. Type 2 alveolar cells are stem cells in adult lung. *J Clin Invest*.
808 2013;123(7):3025–3036.

809 11. Gokey JJ. YAP regulates alveolar epithelial cell differentiation and AGER via
810 NFIB/KLF5/NKX2-1. *OPEN ACCESS*;23.

811 12. Little DR, et al. Differential chromatin binding of the lung lineage transcription factor NKX2-
812 1 resolves opposing murine alveolar cell fates in vivo. *Nat Commun*. 2021;12(1):2509.

813 13. Penkala IJ, et al. Age-dependent alveolar epithelial plasticity orchestrates lung homeostasis
814 and regeneration. *Cell Stem Cell*. 2021;S1934590921001843.

815 14. Zepp JA, Morrisey EE. Cellular crosstalk in the development and regeneration of the
816 respiratory system. *Nat Rev Mol Cell Biol*. 2019;20(9):551–566.

817 15. Brownfield DG, et al. Alveolar cell fate selection and lifelong maintenance of AT2 cells by
818 FGF signaling. *Nat Commun*. 2022;13(1):7137.

819 16. Liberti DC. Klf5 defines alveolar epithelial type 1 cell lineage commitment during lung
820 development and regeneration.

17. Kaiser AM, et al. p53 governs an AT1 differentiation programme in lung cancer suppression. *Nature*. 2023;619(7971):851–859.

18. Shiraishi K, et al. Biophysical forces mediated by respiration maintain lung alveolar epithelial cell fate. *Cell*. 2023;186(7):1478-1492.e15.

19. Burgess CL, et al. Generation of human alveolar epithelial type I cells from pluripotent stem cells. *Cell Stem Cell*. 2024;S1934590924000985.

20. Ohnishi Y, et al. Screening of factors inducing alveolar type 1 epithelial cells using human pluripotent stem cells. *Stem Cell Reports*. 2024;19(4):529–544.

21. Pan X, et al. TRβ activation confers AT2-to-AT1 cell differentiation and anti-fibrosis during lung repair via KLF2 and CEBPA. *Nat Commun*. 2024;15(1):8672.

22. Desai TJ, Brownfield DG, Krasnow MA. Alveolar progenitor and stem cells in lung development, renewal and cancer. *Nature*. 2014;507(7491):190–194.

23. Li J, et al. The Strength of Mechanical Forces Determines the Differentiation of Alveolar Epithelial Cells. *Developmental Cell*. 2018;44(3):297-312.e5.

24. Warren R, et al. Cell competition drives bronchiolization and pulmonary fibrosis. *Nat Commun*. 2024;15(1):10624.

25. Finn J, et al. Dlk1-Mediated Temporal Regulation of Notch Signaling Is Required for Differentiation of Alveolar Type II to Type I Cells during Repair. *Cell Rep*. 2019;26(11):2942-2954.e5.

840 26. Liu Z, et al. MAPK-Mediated YAP Activation Controls Mechanical-Tension-Induced
841 Pulmonary Alveolar Regeneration. *Cell Reports*. 2016;16(7):1810–1819.

842 27. Jiang P, et al. Ineffectual Type 2–to–Type 1 Alveolar Epithelial Cell Differentiation in
843 Idiopathic Pulmonary Fibrosis: Persistence of the KRT8 ^{hi} Transitional State. *Am J Respir Crit*
844 *Care Med*. 2020;201(11):1443–1447.

845 28. Zhou B, et al. Claudin-18-mediated YAP activity regulates lung stem and progenitor cell
846 homeostasis and tumorigenesis. *J Clin Invest*. 2018;128(3):970–984.

847 29. Kobayashi Y. Persistence of a regeneration-associated, transitional alveolar epithelial cell
848 state in pulmonary fibrosis. *Nature Cell Biology*. 2020;35.

849 30. Strunz M, et al. Alveolar regeneration through a Krt8+ transitional stem cell state that
850 persists in human lung fibrosis. *Nat Commun*. 2020;11(1):3559.

851 31. Konkimalla A, et al. Transitional cell states sculpt tissue topology during lung regeneration.
852 *Cell Stem Cell*. 2023;30(11):1486-1502.e9.

853 32. Choi J, et al. Inflammatory Signals Induce AT2 Cell-Derived Damage-Associated Transient
854 Progenitors that Mediate Alveolar Regeneration. *Cell Stem Cell*. 2020;27(3):366-382.e7.

855 33. Ke X, et al. Morphogenesis and regeneration share a conserved core transition cell state
856 program that controls lung epithelial cell fate. *Developmental Cell*. 2024;S1534580724006993.

34. Katsura H, et al. Human Lung Stem Cell-Based Alveolospheres Provide Insights into SARS-CoV-2-Mediated Interferon Responses and Pneumocyte Dysfunction. *Cell Stem Cell*. 2020;27(6):890-904.e8.

35. Rogalski AA, Singer SJ. Associations of elements of the Golgi apparatus with microtubules. *The Journal of cell biology*. 1984;99(3):1092–1100.

36. Chabin-Brion K, et al. The Golgi Complex Is a Microtubule-organizing Organelle. *MBoC*. 2001;12(7):2047–2060.

37. Nakamura N, et al. Characterization of a cis-Gol Matrix Protein, GM130.

38. Fu M, et al. The Golgi Outpost Protein TPPP Nucleates Microtubules and Is Critical for Myelination. *Cell*. 2019;179(1):132-146.e14.

39. Ori-McKenney KM, Jan LY, Jan Y-N. Golgi Outposts Shape Dendrite Morphology by Functioning as Sites of Acentrosomal Microtubule Nucleation in Neurons. *Neuron*. 2012;76(5):921–930.

40. Piperno G, LeDizet M, Chang X. Microtubules Containing Acetylated a-Tubulin in Mammalian Cells in Culture. *The Journal of Cell Biology*. 1987;104.

41. Hutchison V, et al. Inducible tricolor reporter mouse for parallel imaging of lysosomes, mitochondria, and microtubules. *Journal of Cell Biology*. 2024;223(1):e202305086.

42. Mitchison T, Kirschner M. Dynamic instability of microtubule growth. *Nature*. 1984;312(5991):237–242.

876 43. Bauer NG, Richter-Landsberg C, Ffrench-Constant C. Role of the oligodendroglial
877 cytoskeleton in differentiation and myelination. *Glia*. 2009;57(16):1691–1705.

878 44. Grundke-Iqbal I, et al. Abnormal phosphorylation of the microtubule-associated protein tau
879 (tau) in Alzheimer cytoskeletal pathology. *Proc Natl Acad Sci USA*. 1986;83(13):4913–4917.

880 45. Wang Y, Mandelkow E. Tau in physiology and pathology. *Nat Rev Neurosci*. 2016;17(1):22–
881 35.

882 46. Doench JG, et al. Optimized sgRNA design to maximize activity and minimize off-target
883 effects of CRISPR-Cas9. *Nat Biotechnol*. 2016;34(2):184–191.

884 47. Hsiau T, et al. *Inference of CRISPR Edits from Sanger Trace Data*. Bioinformatics; 2018.

885 48. Chiou S-H, et al. Pancreatic cancer modeling using retrograde viral vector delivery and in
886 vivo CRISPR/Cas9-mediated somatic genome editing. *Genes Dev*. 2015;29(14):1576–1585.

887 49. Wegmann S, et al. Tau protein liquid-liquid phase separation can initiate tau aggregation.
888 *EMBO J*. 2018;37(7):e98049.

889 50. Hernández-Vega A, et al. Local Nucleation of Microtubule Bundles through Tubulin
890 Concentration into a Condensed Tau Phase. *Cell Reports*. 2017;20(10):2304–2312.

891 51. Lewis J, et al. Neurofibrillary tangles, amyotrophy and progressive motor disturbance in
892 mice expressing mutant (P301L) tau protein. *Nat Genet*. 2000;25(4):402–405.

893 52. Spillantini MG, et al. Tau Pathology in Two Dutch Families with Mutations in the
894 Microtubule-Binding Region of Tau. *The American Journal of Pathology*. 1998;153(5):1359–
895 1363.

896 53. Wegmann S, et al. Experimental evidence for the age dependence of tau protein spread in
897 the brain. *Sci Adv*. 2019;5(6):eaaw6404.

898 54. Dawson HN. Delayed axonogenesis in tau deficient neurons. 2001;9.

899 55. Konkimalla A, et al. Efficient AAV Mediated Transgenesis in Alveolar Stem Cells and
900 Associated Niches. *Am J Respir Cell Mol Biol*. 2023;rcmb.2022-0424MA.

901 56. Farmer KM, et al. P53 aggregation, interactions with tau, and impaired DNA damage
902 response in Alzheimer's disease. *acta neuropathol commun*. 2020;8(1):132.

903 57. Cross SM, et al. A p53-Dependent Mouse Spindle Checkpoint. *Science*.
904 1995;267(5202):1353–1356.

905 58. Giannakakou P, et al. p53 is associated with cellular microtubules and is transported to the
906 nucleus by dynein. *Nat Cell Biol*. 2000;2(10):709–717.

907 59. Kim N, et al. Single-cell RNA sequencing demonstrates the molecular and cellular
908 reprogramming of metastatic lung adenocarcinoma. *Nat Commun*. 2020;11(1):2285.

909 60. Fingerlin TE, et al. Genome-wide association study identifies multiple susceptibility loci for
910 pulmonary fibrosis-supplement data file. *Nat Genet*. 2013;45(6):613–620.

911 61. Allen RJ, et al. Genome-Wide Association Study of Susceptibility to Idiopathic Pulmonary
912 Fibrosis. *Am J Respir Crit Care Med*. 2020;201(5):564–574.

913 62. Allen RJ, et al. Genetic variants associated with susceptibility to idiopathic pulmonary
914 fibrosis in people of European ancestry: a genome-wide association study. *Lancet Respir Med*.
915 2017;5(11):869–880.

916 63. Hobbs BD, et al. Genetic loci associated with chronic obstructive pulmonary disease overlap
917 with loci for lung function and pulmonary fibrosis. *Nat Genet*. 2017;49(3):426–432.

918 64. Wain LV, et al. Genome-wide association analyses for lung function and chronic obstructive
919 pulmonary disease identify new loci and potential druggable targets. *Nat Genet*.
920 2017;49(3):416–425.

921 65. Stefansson H, et al. A common inversion under selection in Europeans. *Nat Genet*.
922 2005;37(2):129–137.

923 66. Weibel ER. On the Tricks Alveolar Epithelial Cells Play to Make a Good Lung. *Am J Respir Crit*
924 *Care Med*. 2015;191(5):504–513.

925 67. Chen J, et al. Projection domains of MAP2 and tau determine spacings between
926 microtubules in dendrites and axons. *Nature*. 1992;360(6405):674–677.

927 68. Lewis SA, Cowan N. Microtubule bundling. *Nature*. 1990;345(6277):674.

928 69. Choi C-S, et al. Cytotoxic tau released from lung microvascular endothelial cells upon
929 infection with Pseudomonas aeruginosa promotes neuronal tauopathy. *Journal of Biological*
930 *Chemistry*. 2022;298(1):101482.

931 70. Balczon R, et al. Pneumonia initiates a tauopathy. *FASEB J*. 2021;35(9):e21807.

932 71. Strang KH, Golde TE, Giasson BI. MAPT mutations, tauopathy, and mechanisms of
933 neurodegeneration. *Laboratory Investigation*. 2019;99(7):912–928.

934 72. LoPresti P, et al. Functional implications for the microtubule-associated protein tau:
935 localization in oligodendrocytes. *Proc Natl Acad Sci USA*. 1995;92(22):10369–10373.

936 73. McKenna ED, et al. The Tubulin Code, from Molecules to Health and Disease. *Annu Rev Cell*
937 *Dev Biol*. 2023;39(1):331–361.

938 74. Roll-Mecak A. The Tubulin Code in Microtubule Dynamics and Information Encoding.
939 *Developmental Cell*. 2020;54(1):7–20.

940 75. Janke C, Magiera MM. The tubulin code and its role in controlling microtubule properties
941 and functions. *Nat Rev Mol Cell Biol*. 2020;21(6):307–326.

942 76. Jijumon AS, et al. Lysate-based pipeline to characterize microtubule-associated proteins
943 uncovers unique microtubule behaviours. *Nat Cell Biol*. 2022;24(2):253–267.

944 77. Natri HM, et al. *Cell type-specific and disease-associated eQTL in the human lung*. Genomics;
945 2023.

946 78. Rock JR, et al. Multiple stromal populations contribute to pulmonary fibrosis without
947 evidence for epithelial to mesenchymal transition. *Proceedings of the National Academy of*
948 *Sciences*. 2011;108(52):E1475–E1483.

949 79. Madisen L, et al. A robust and high-throughput Cre reporting and characterization system
950 for the whole mouse brain. *Nat Neurosci*. 2010;13(1):133–140.

951 80. Marino S, et al. Induction of medulloblastomas in *p53* -null mutant mice by somatic
952 inactivation of *Rb* in the external granular layer cells of the cerebellum. *Genes Dev*.
953 2000;14(8):994–1004.

954 81. Konishi S, Tata A, Tata PR. Defined conditions for long-term expansion of murine and human
955 alveolar epithelial stem cells in three-dimensional cultures. *STAR Protocols*. 2022;3(2):101447.

956 82. Kadur Lakshminarasimha Murthy P, et al. Human distal lung maps and lineage hierarchies
957 reveal a bipotent progenitor. *Nature*. 2022;604(7904):111–119.

958 83. Labun K, et al. CHOPCHOP v3: expanding the CRISPR web toolbox beyond genome editing.
959 *Nucleic Acids Research*. 2019;47(W1):W171–W174.

960 84. Martin M. Cutadapt removes adapter sequences from high-throughput sequencing reads.
961 *EMBnet.journal*. 2011;17(1):10–12.

962 85. Bolger AM, Lohse M, Usadel B. Trimmomatic: a flexible trimmer for Illumina sequence data.
963 *Bioinformatics*. 2014;30(15):2114–2120.

86. Love MI, Huber W, Anders S. Moderated estimation of fold change and dispersion for RNA-seq data with DESeq2. *Genome Biology*. 2014;15(12):550.

87. Sajuthi SP, et al. Nasal airway transcriptome-wide association study of asthma reveals genetically driven mucus pathobiology. *Nat Commun*. 2022;13(1):1632.

88. Lewis MJ, Wang S. locuszoomr: an R package for visualizing publication-ready regional gene locus plots. *Bioinform Adv*. 2025;5(1):vbaf006.

89. Myers TA, Chanock SJ, Machiela MJ. LDlinkR: An R Package for Rapidly Calculating Linkage Disequilibrium Statistics in Diverse Populations. *Front Genet*. 2020;11:157.

90. Konkimalla A, et al. Multi-apical polarity of alveolar stem cells and their dynamics during lung development and regeneration. *iScience*. 2022;105114.

Figures

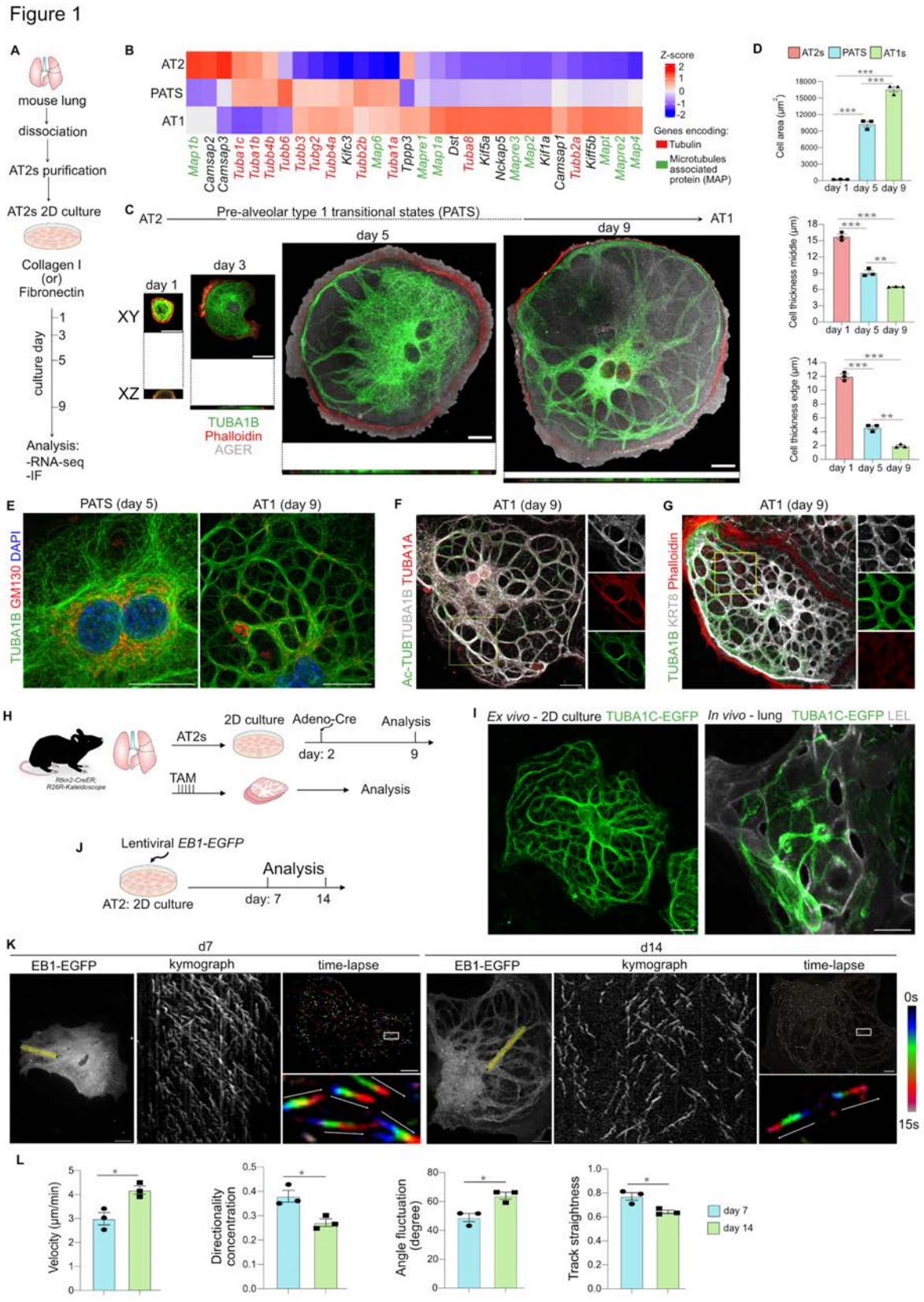
Figure 1
A
mouse lung
dissociation
AT2s purification
AT2s 2D culture
Collagen I
(or)
Fibronectin
culture day
1
3
5
9
Analysis:
-RNA-seq
-IF
B
AT2
PATS
AT1
Map1b
Camsap2
Camsap3
Tuba1c
Tuba1b
Tubb4b
Tubb6
Tubb3
Tubg2
Tubb4a
Kifc3
Tubb2b
Map6
Tuba1a
Tppp3
Mapre1
Map1a
Dst
Tuba8
Kif5a
Nckap5
Mapre3
Map2
Kif1a
Camsap1
Tubb2a
Kiff5b
Mapt
Mapre2
Map4
Z-score
2
1
0
-1
-2
Genes encoding:
Tubulin
Microtubules associated protein (MAP)
C
AT2
Pre-alveolar type 1 transitional states (PATS)
AT1
day 1
day 3
day 5
day 9
XY
XZ
TUBA1B
Phalloidin
AGER
D
AT2s
PATS
AT1s
Cell area (μm²)
Cell thickness middle (μm)
Cell thickness edge (μm)
day 1
day 5
day 9
E
PATS (day 5)
AT1 (day 9)
TUBA1B GM130 DAPI
F
AT1 (day 9)
Ac-TUB TUBA1B TUBA1A
G
AT1 (day 9)
TUBA1B KRT8 Phalloidin
H
Rtkn2-CreER;
R26R-Kaleidoscope
AT2s
2D culture
Adeno-Cre
Analysis
day: 2
9
TAM
Analysis
I
Ex vivo - 2D culture TUBA1C-EGFP
In vivo - lung TUBA1C-EGFP LEL
J
Lentiviral EB1-EGFP
AT2: 2D culture
Analysis
day: 7
14
K
d7
d14
EB1-EGFP
kymograph
time-lapse
0s
15s
L
Velocity (μm/min)
Directionality concentration
Angle fluctuation (degree)
Track straightness
day 7
day 14

Figure 1: Alveolar stem cell microtubules undergo dynamic changes to form thick MT bundles during differentiation. (A) Experimental design for mouse AT2 isolation, culture and sample collection. (B) Heatmap shows expression of tubulin-encoding and MAP encoding genes in cultured AT2s, PATS and AT1s. (C) Staining for TUBA1B (green) phalloidin (red) and AGER (grey) on cells cultured on fibronectin showing AT2-PATS-AT1 cell fate and cell morphology transition. Scale bar: 20μm. (D) Quantification of area and thickness (in the middle and edge) of alveolar epithelial cells on day-1, 5 and 9 of culture. $^{**}p \leq 0.005$, $^{***}p < 0.001$, one-way ANOVA. n=3 biological replicates. (E) Staining for TUBA1B (green) and GM130 (red) at indicated times. Scale bar: 20μm. (F) Staining for tubulin proteins in AT2s cultured on fibronectin for 9-days. Scale bar: 20μm. (G) Staining for TUBA1B (green), KRT8 (grey) and phalloidin (red) in AT1s. Scale bar: 20μm. (H) Experimental design for *ex vivo* and *in vivo* AT1-specific tubulin lineage tracing in *Rtkn2-CreER;R26R-Kaleidoscope* mice. (I) Images showing TUBA1C-EGFP in cultured AT1s and *in vivo* lungs. Scale bars: 20μm. (J) Experimental workflow for AT2 infection with *EB1-EGFP* lentivirus followed by live imaging on day-7 and day-14. (K) Kymograph and time-lapse images illustrating tubulin dynamics and orientation in cells on day-7 and day-14. Scale bars: 20μm. (L) Quantification of EB1-EGFP comet velocity (μm/min), directionality concentration, angle fluctuation (degree) and track straightness in cells cultured for 7 and 14 days. $^{*}p < 0.05$, unpaired t-test. Data in D and L are presented as mean ± s.e.m. n=3 biological replicates.

Figure 2

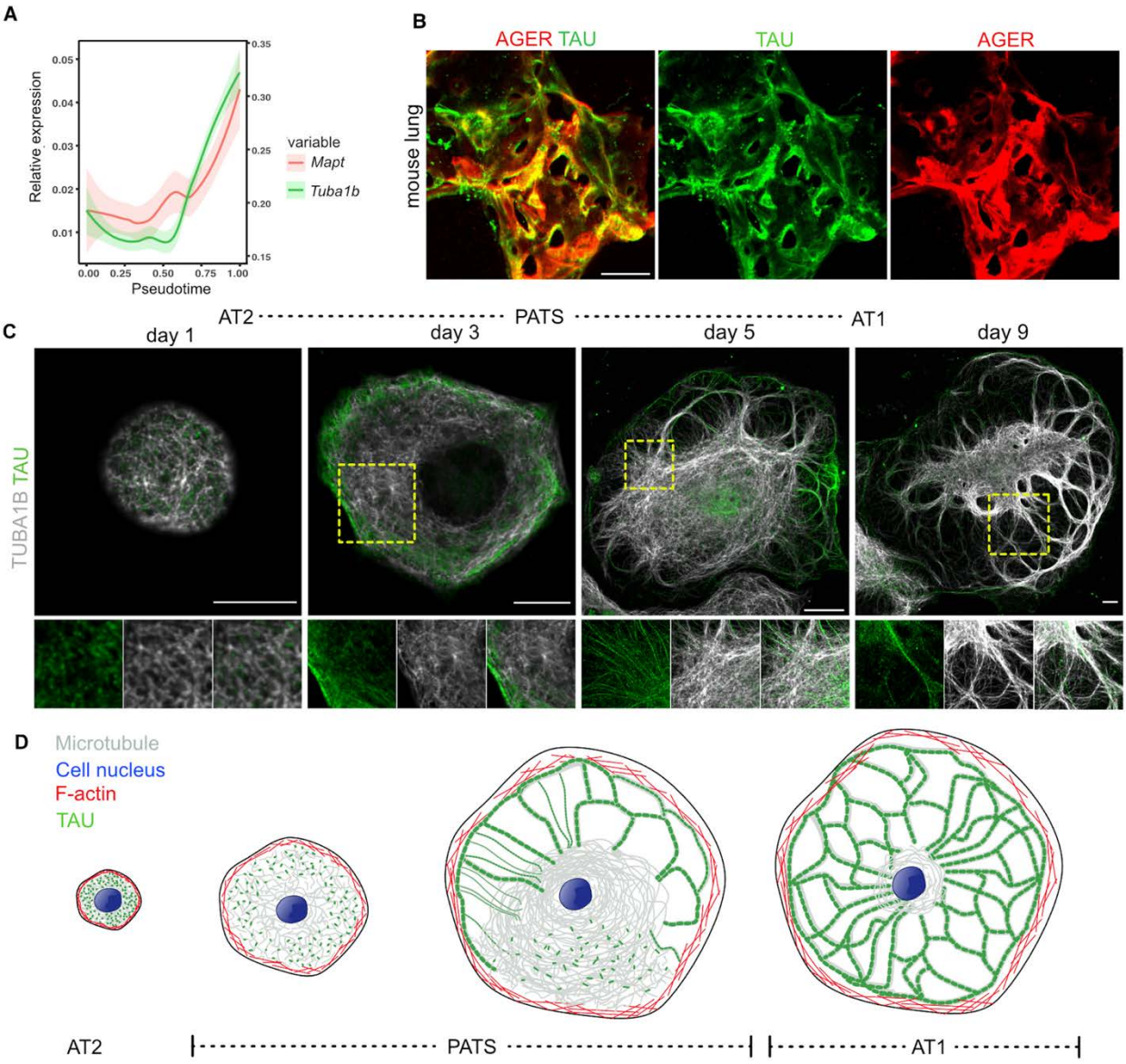

Figure 2. Dynamic expression and localization of TAU precede thick MT-bundles formation during AT2 differentiation. (A) Pseudo time analysis visualizing gene expression dynamics of *Mapt* and *Tuba1b* during AT2-AT1 differentiation. (B) Immunostaining for AGER (red) and TAU (green) in the alveolar region of a thick tissue section showing TAU localization in AT1s. Scale bar: 20µm. (C) Staining for TUBA1B (grey) and TAU (green) at indicated times of culture. Scale bars: 20µm. Yellow box indicates region of single-channel images. (D) Schematic showing the expression and organization of TAU, microtubules, and F-actin during AT2-AT1 differentiation.

Figure 3

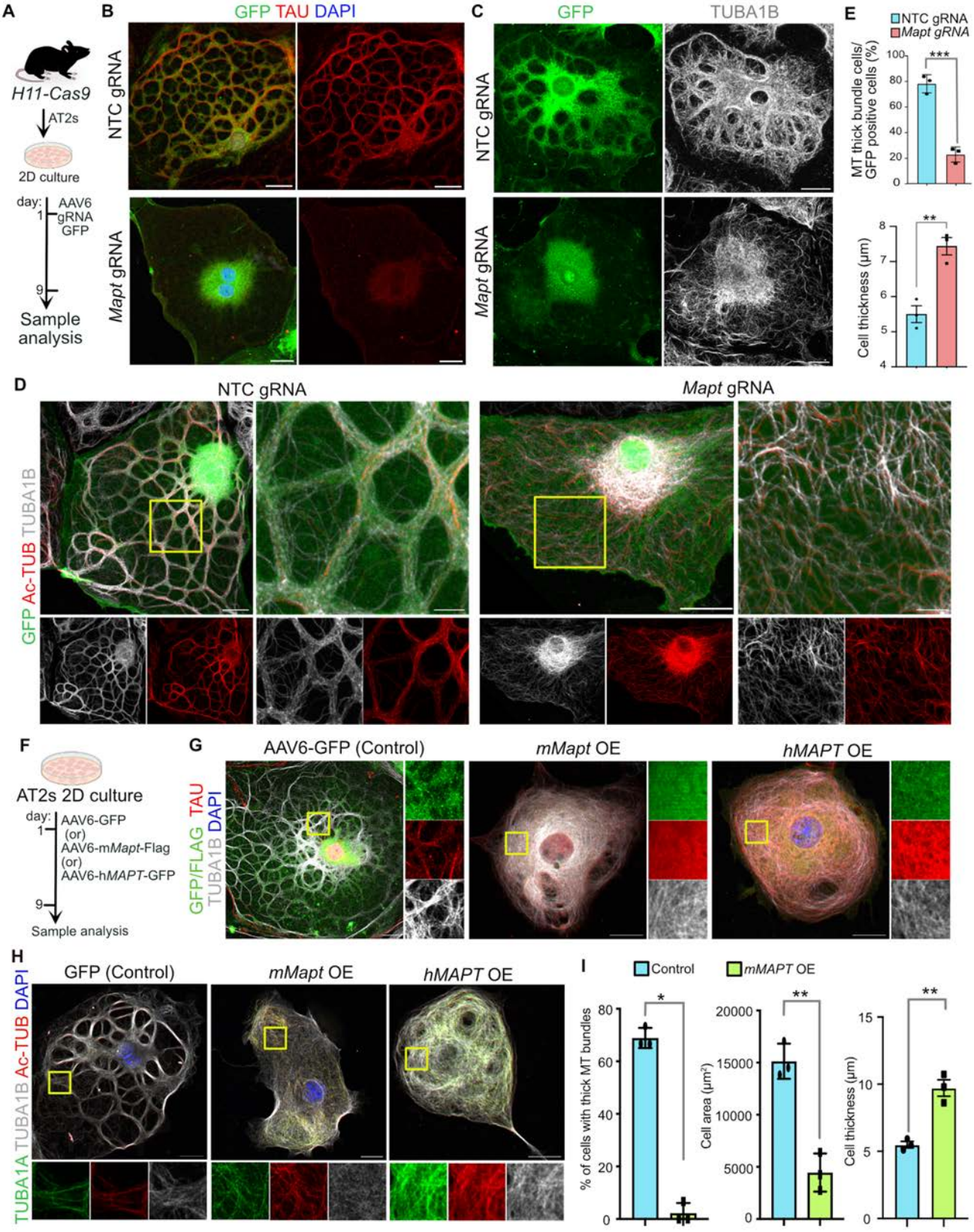

1024

Figure 3. TAU regulates the formation of thick MT-bundles. (A) Experimental design for AT2 isolation from *H11-Cas9* mice followed by AT2 culture and *AAV6-gRNA-GFP* infection to knockout (KO) *Mapt ex vivo*. (B) Staining for GFP (green, infected cells) and TAU (red)I in NTC (non-targeting control) and *Mapt-KO* cells. Scale bars: 20μm. (C) Staining for GFP (green) and TUBA1B (grey) in control and *Mapt*-KO cells. Scale bars: 20μm. (D) Staining for TUBA1B (grey) and Ac-TUB (red) in infected GFP^+ (green) control and *Mapt*-deleted cells. Scale bars: 20μm (low magnification); 5μm (high magnification). Yellow box indicates region of single-channel images. (E) Quantification of cells exhibiting thick MT-bundles and cell thickness in control and *Mapt*-deleted cells. ***p*=0.0049, ***p=0.0005 unpaired t-test, n=3 biological replicates. (F) Schematic of *ex vivo* cultured AT2s infected with mouse *Mapt* or human *MAPT* and analyses at indicated time point. (G) Staining for TAU (red) and TUBA1B (grey) in control and TAU-overexpressed cell (green). Scale bars: 20μm. Yellow box indicates region of single-channel images. DAPI stains nuclei (blue). (H) Staining for TUBA1A (green), TUBA1B (grey) and Ac-TUB (red) in TAU-overexpressed and control cells. (I) Quantification of cell area, cell thickness and the percentage of infected cells exhibiting thick MT-bundles. **p*=0.05, Mann Whitney statistical test. ***p*<0.005, unpaired t-test, n=3 biological replicates. Data in E and I are presented as mean ± s.e.m.

Figure 4

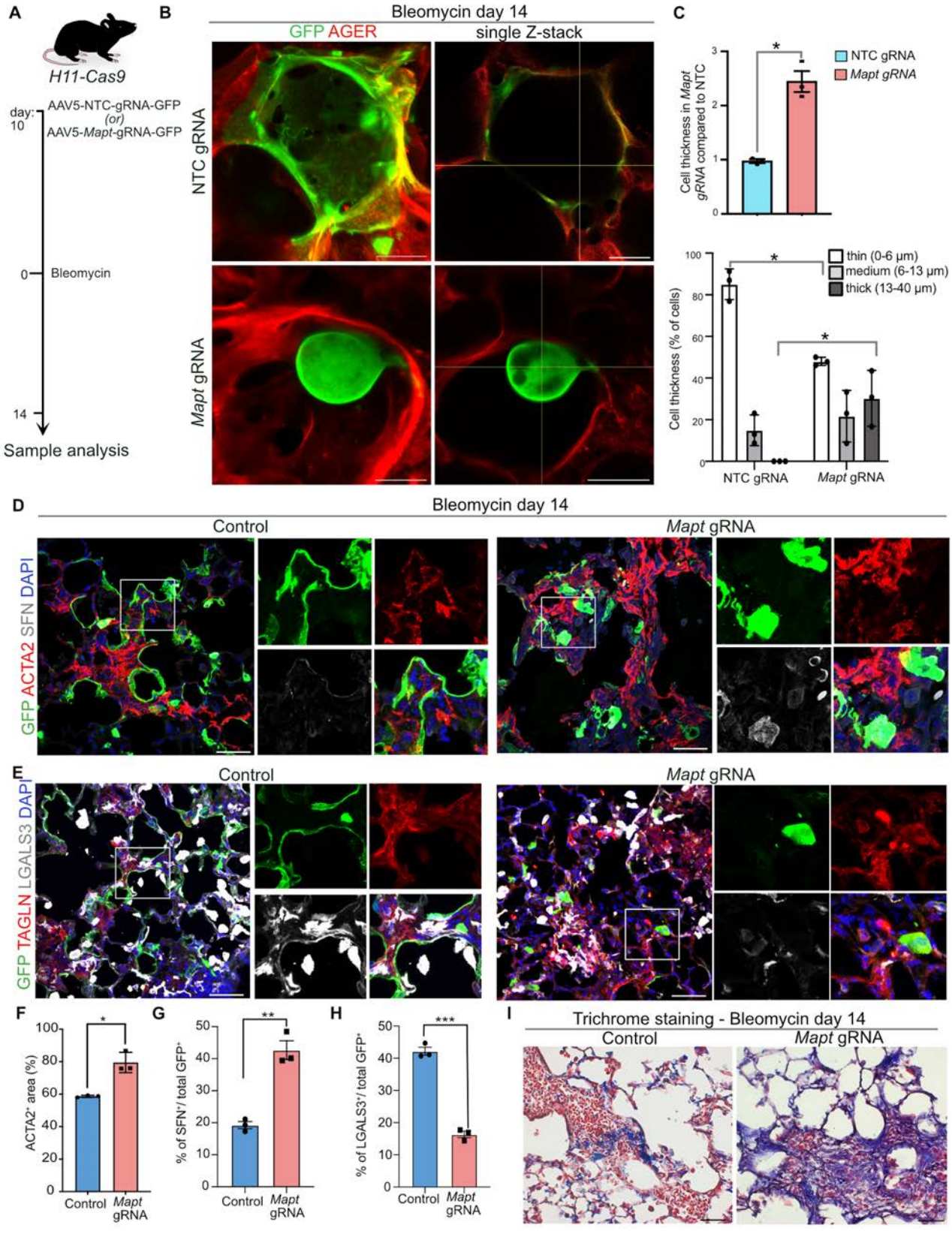

1052

Figure 4. Loss of *Mapt* leads to abnormal cell organization and increased fibrosis in response to bleomycin injury. (A) Schematic of AT2-specific gRNA delivery to *H11-Cas9* mice followed by bleomycin injury and sample collection. (B) Staining for GFP (green, gRNA delivered AT2s) and AGER (red) in control and *Mapt*-deleted cells after bleomycin injury. Scale bars: 20μm. (C) Quantification of cell thickness and the distribution of GFP^+ cells with different thickness in control and AT2-specific *Mapt-KO* lungs after bleomycin injury. *$p<0.05$, unpaired two-tailed t-test. (D) Staining for GFP (green), ACTA2 (red) and SFN (grey) in controls and *Mapt*-deleted AT2s after bleomycin injury. Scale bars: 50μm. (E) Staining for GFP (green), TAGLN (red), and LGALS3 (grey) in controls and *Mapt*-deleted AT2s after bleomycin injury. Scale bars: 50μm. DAPI stains nuclei (blue). (F) Quantification on $ACTA2^+$ area in bleomycin-injured lungs. *$p<0.05$ unpaired t-test. (G) Quantification of SFN^+ cells among GFP^+ cells in bleomycin-injured lungs. **$p<0.005$, unpaired t-test. (H) Quantification of $LGALS3^+$ cells among GFP^+ cells in bleomycin-injured lungs. ***$p\leq0.001$, unpaired t-test. (I) Trichrome staining on lungs collected from bleomycin-injured controls and *Mapt*-deleted mice. Scale bars: 100μm. Data in C, F, G and H are presented as mean ± s.e.m. n=3 biological replicates.

Figure 5

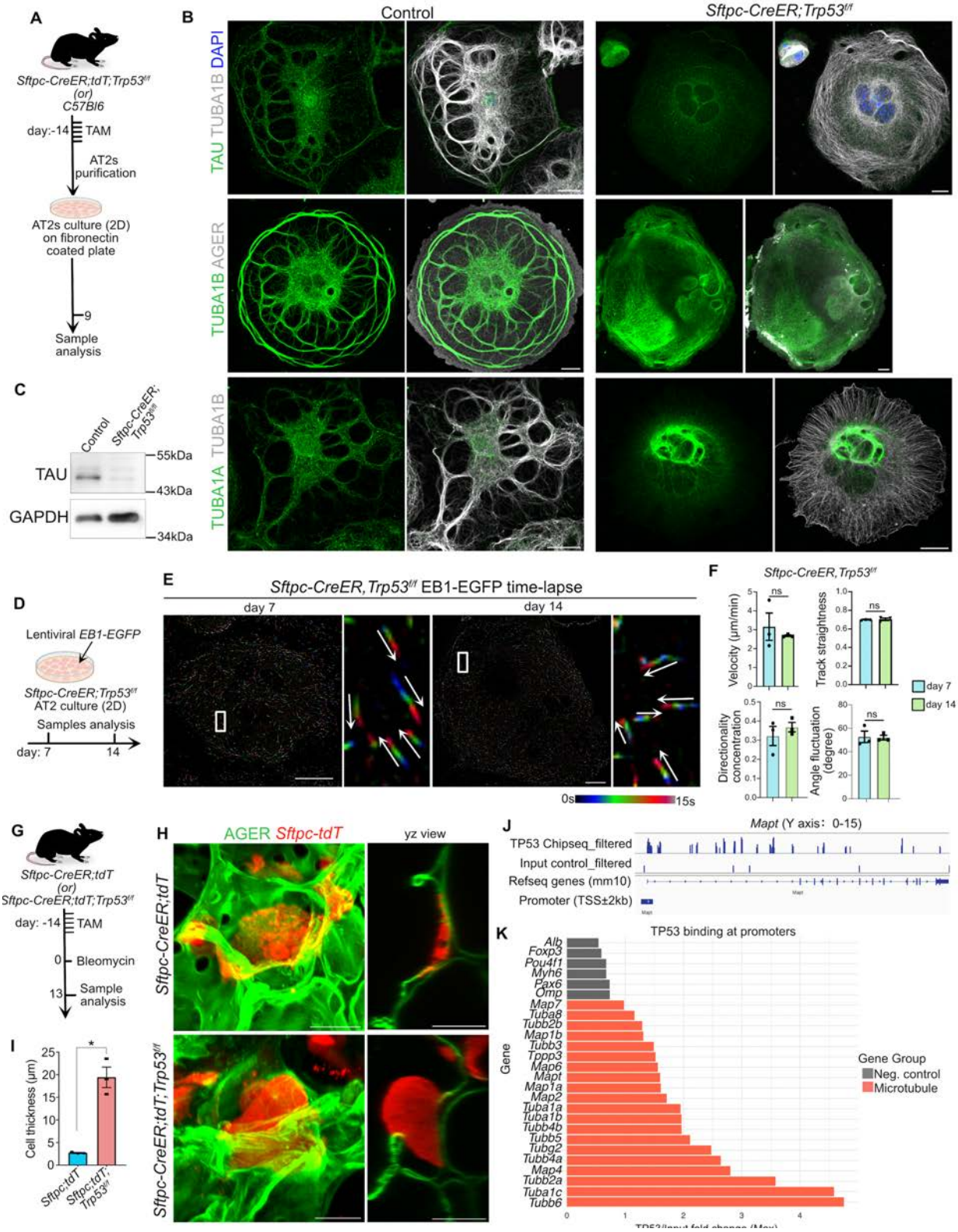

1070

Figure 5. Loss of TP53 disrupts microtubule organization and AT1 differentiation. (A) Experimental workflow for tamoxifen administration to delete TP53 in AT2s followed by AT2s isolation for *ex vivo* analysis in *Sftpc-CreER;R26R-tdTomato;Trp53*$^{f/f}$ or control mice. (B) Images showing TAU and tubulin localization in control and TP53-deleted cells. Scale bars: 20μm. DAPI stains nuclei (blue). (C) Western blot of TAU and GAPDH (loading control) in control and TP53-deleted cells. (D) Experimental design for *EB1-EGFP* lentivirus administration in TP53-deleted AT2s followed by live imaging on days-7 and 14. (E) Kymograph and time-lapse images for EB1-EGFP in *Trp53*-deleted cells on days-7 and 14 of culture. (F) Quantification of EB1-EGFP comet velocity (μm/min), directionality concentration, angle fluctuation (degree) and track straightness in TP53-deleted cells cultured for 7 and 14 days. ns - not significant, unpaired t-test. (G) Experimental workflow for tamoxifen administration to delete TP53 in AT2s followed by bleomycin injury in *Sftpc-tdT-Trp53-KO* or control mice (*Sftpc-tdT).* (H) Staining for AGER (green) and tdTomato (red) in bleomycin-injured controls and *Trp53-KO* mice. Scale bars: 20μm. (I) Quantification on cell thickness of lineage labelled cells in controls and *Trp53-KO* mice following bleomycin injury. **p*=0.017, unpaired t-test. (J) IGV tracks show significant enrichment for TP53 binding in genomic loci corresponding to *Mapt* promoter. (K) Graph depicting enrichment of TP53 binding on microtubule associated genes (red) and unrelated negative controls (grey). Data in F and I are presented as mean ± s.e.m. n=3 biological replicates

Figure 6

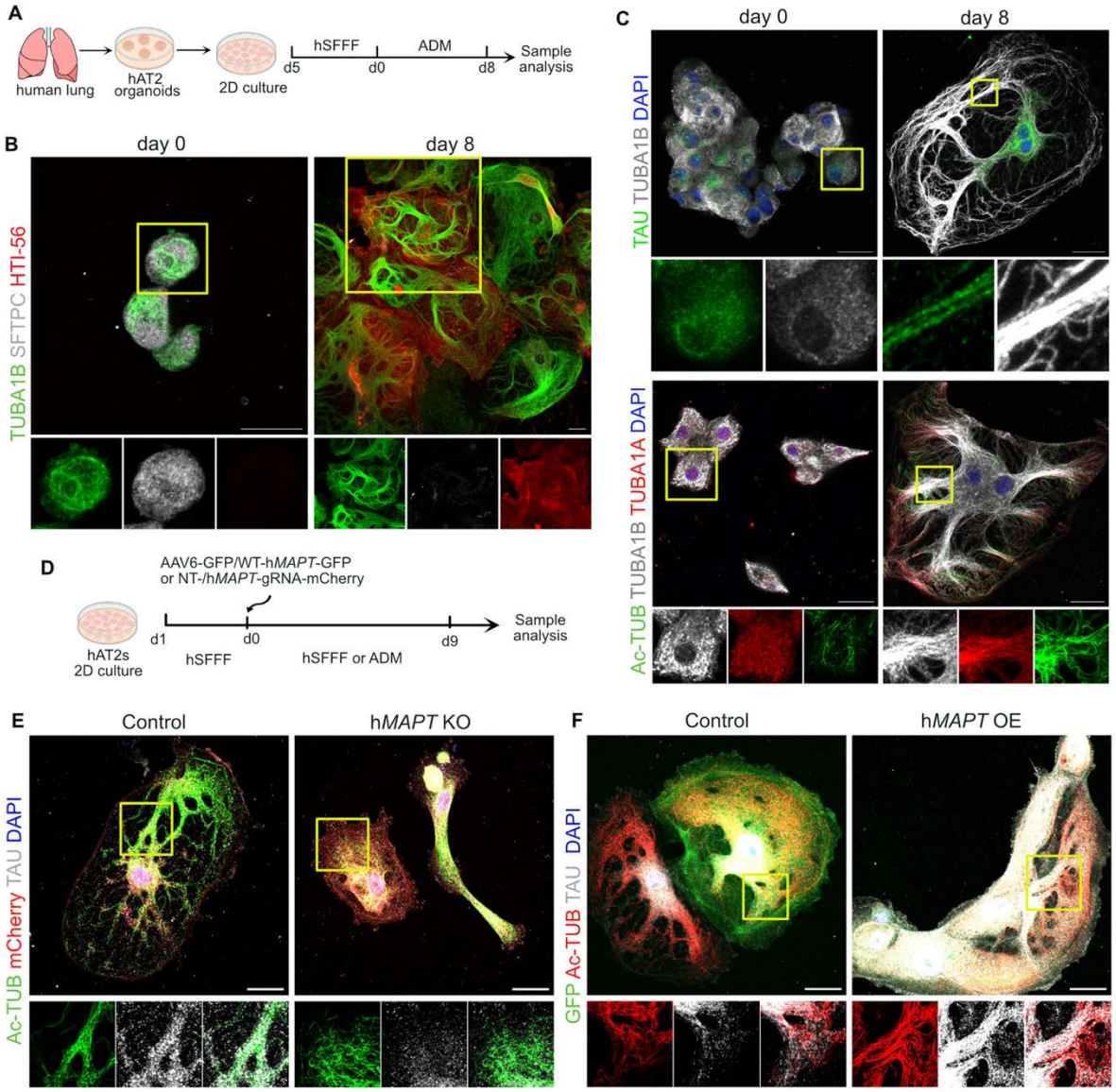

Figure 6. *MAPT* regulates human AT2 differentiation into AT1s. (A) Schematic of human AT2 purification, culture and differentiation followed by analyses. B) Staining for TUBA1B (green) , SFTPC (grey) and HTI-56 (red) in AT2s and *ex vivo* differentiated AT1s. Scale bars: 20μm. (C) Staining for TAU (green) and TUBA1B (grey) (upper panel) and Ac-TUB (green),TUBA1A (red) and TUBA1B (grey) (lower panel) in AT2s and AT1s. Scale bars: 20μm. (D) Workflow for *MAPT* deletion or overexpression in AT2s followed by differentiation to AT1s and analyses. (E) Staining for Ac-TUB (green) mCherry (red) and TAU (grey) on *MAPT*-deleted and control cells. Scale bars: 20μm. DAPI stains nuclei (blue). (F) Staining for GFP (green), Ac-TUB (red)N and TAU (grey) on *MAPT*-overexpressed and control cells. Scale bars: 20μm. Yellow box in merged image indicates region of single-channel images.

Supplemental Figures

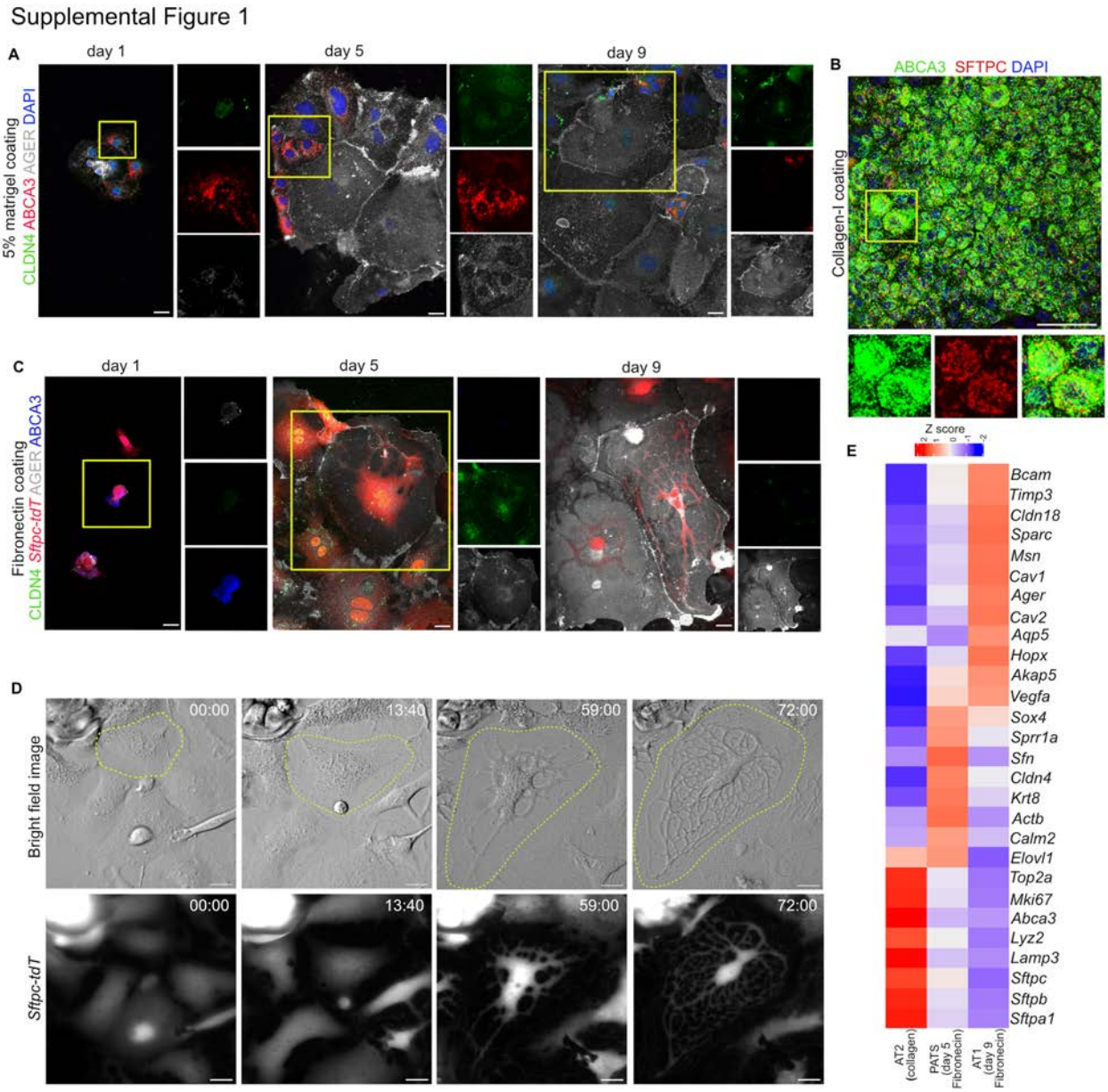

Supplemental Figure 1. The establishment and characterization of *ex vivo* 2D alveolar epithelial cells culture conditions. (A) Immunostaining for CLDN4 (green), ABCA3 (red) and AGER (grey) on alveolar epithelial cells cultured on 5% Matrigel for different days. Scale bars: 20μm. (B) Staining for AT2 markers, ABCA3 (green) and SFTPC (red), in AT2s cultured on Collagen I for 5 days. Scale bar: 50μm. (C) Staining for CLDN4 (green), ABCA3 (blue), and AGER (grey) on AT2s isolated from *Sftpc-CreER;R26R-tdTomato* (red) lungs and cultured on fibronectin for different days. Scale bars: 20μm. (A and B) DAPI stains nuclei (blue). Yellow box indicates

region of single channel images. (D) Time frames showing the expansion of cultured alveolar epithelial cells isolated from over time. Scale bars: 10μm. Yellow dashed line depict expanding cell. (E) Heatmap showing expression of AT2, PATS and AT1 markers in cells collected from indicated culture conditions.

Supplemental Figure 2

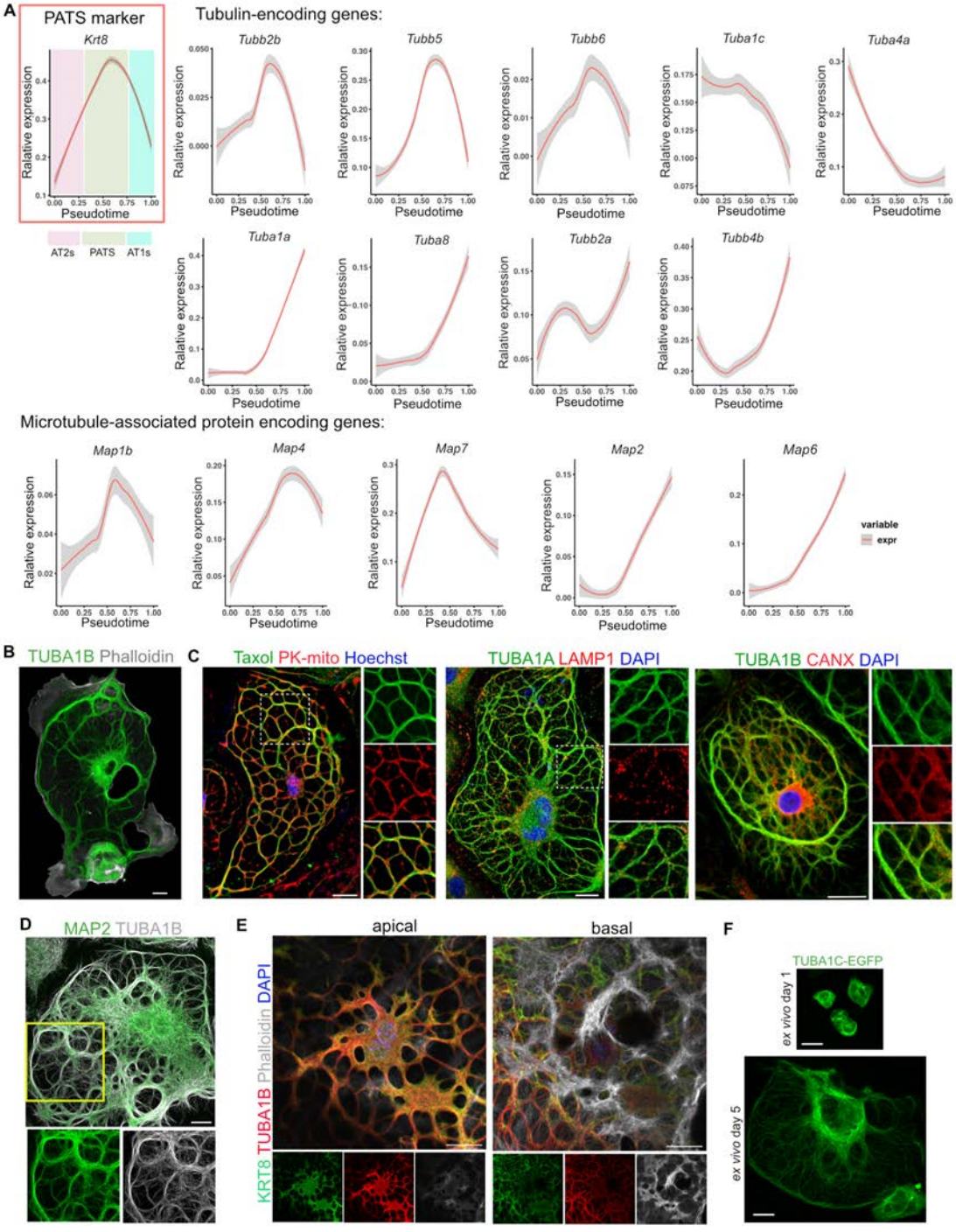

Supplemental Figure 2. Dynamics expression of tubulin-encoding genes and microtubule-associated protein encoding genes during AT2 differentiation to AT1. (A) Pseudotime analysis visualizing expression dynamics of tubulin-encoding genes and microtubule-associated protein encoding genes during AT2-AT1 differentiation. *Krt8* expression is depicting emergence of PATS. The pseudotime for AT2, PATS and AT1s were labelled manually based on expression of *Krt8.* (B) Staining for TUBA1B (green) and phalloidin (grey) in the day 9 cultured cells. Scale bar: 20μm. (C) Staining for Taxol-tubulin (green), PK-mito (red, mitochondria), TUBA1A (green), LAMP1 (red, lysosomes), and CANX (red, endoplasmic reticulum). Hoechst and DAPI stain nuclei (blue). Scale bar: 20μm. (D) Staining for MAP2 (green) and TUBA1B (grey) at day-9 of culture. Scale bar: 20 μm. (E) Images showing localization of KRT8 (green), TUBA1B (red) and phalloidin (grey) on apical and basal side of the AT1s. Scale bar: 20μm. (F) Representative images showing TUBA1C-EGFP in cultured AT2 (culture day-1) and PATS (culture day-5). Scale bars: 20μm.

Supplemental Figure 3

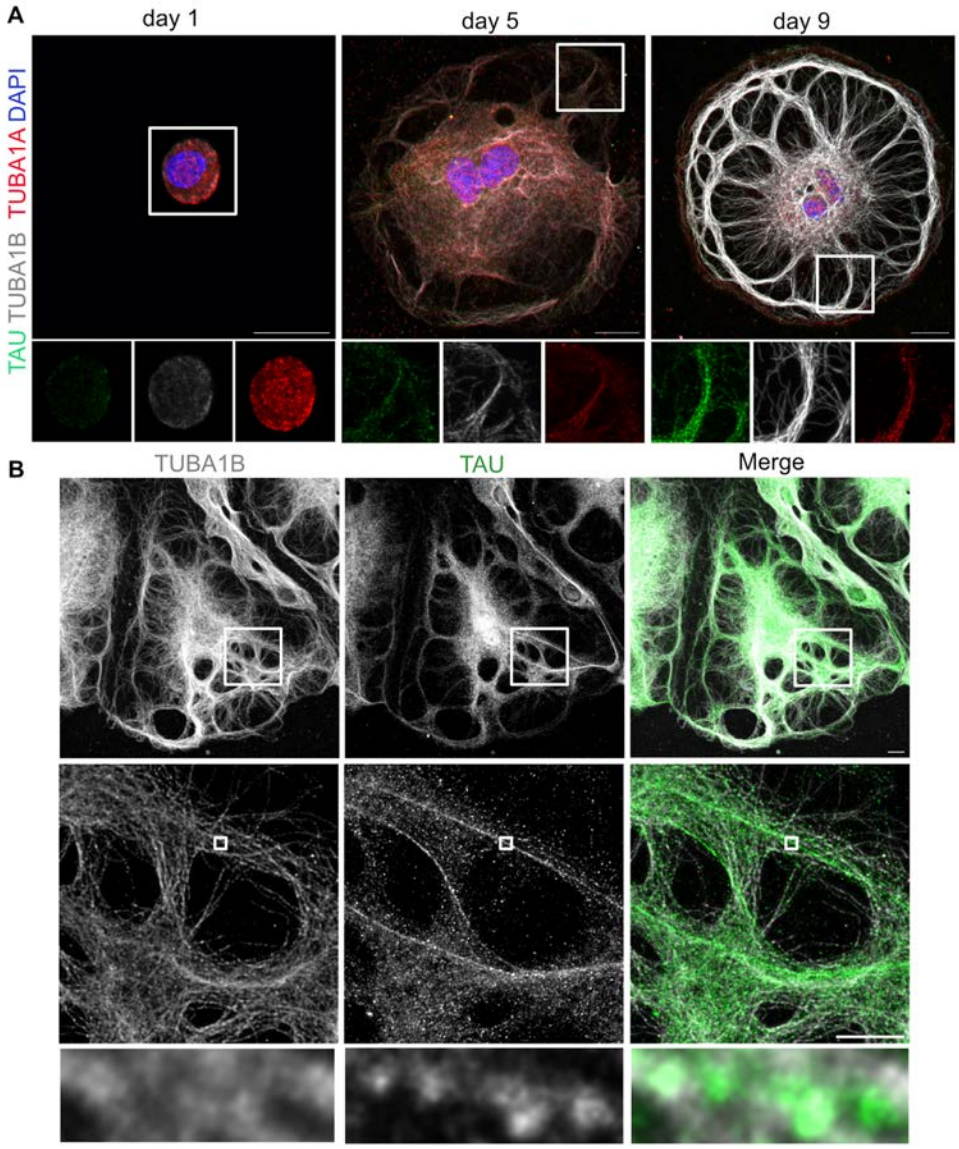

Supplemental Figure 3. Localization of TAU in AT2s and AT1s. (A) Immunostaining for TAU (green), TUBA1B (grey) and TUBA1A (red) during AT2-to-AT1 differentiation. Scale bar: 20μm. (B) Staining for TUBA1B (grey) and TAU (green) in AT1s. Scale bars: 20μm. White box in merged image indicates region of single channel images.

Supplemental Figure 4

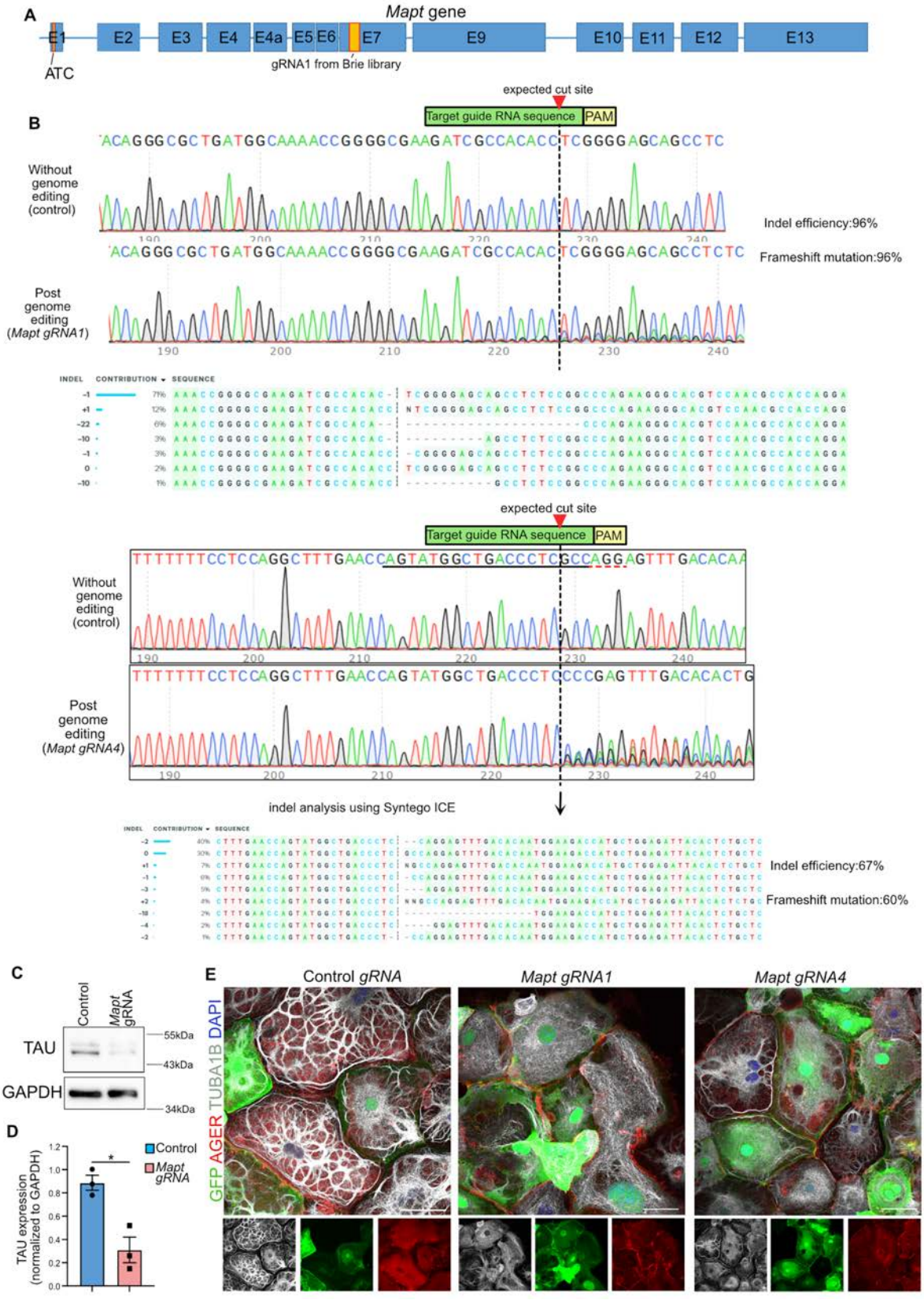

1147

Supplemental Figure 4. Characterization of mouse *Mapt* gRNA efficiency. (A) Schematic of *Mapt* gene. (B) Representative Sanger chromatograms and indel efficiency analysis in controls and *Mapt gRNA1* and *Mapt gRNA4* edited cells. (C) Western blot of TAU in control and *Mapt*-deleted cells. GAPDH was used as a loading control. (D) Quantification of TAU expression in control and *Mapt*-deleted cells. **p*<0.05, unpaired t-test. n=3 biological replicates. (E) Staining for GFP (green, gRNA delivered AT2s) and AGER (red) and TUBA1B (grey) in control and *Mapt*-deleted AT2s. Scale bars: 50μm.

Supplemental Figure 5

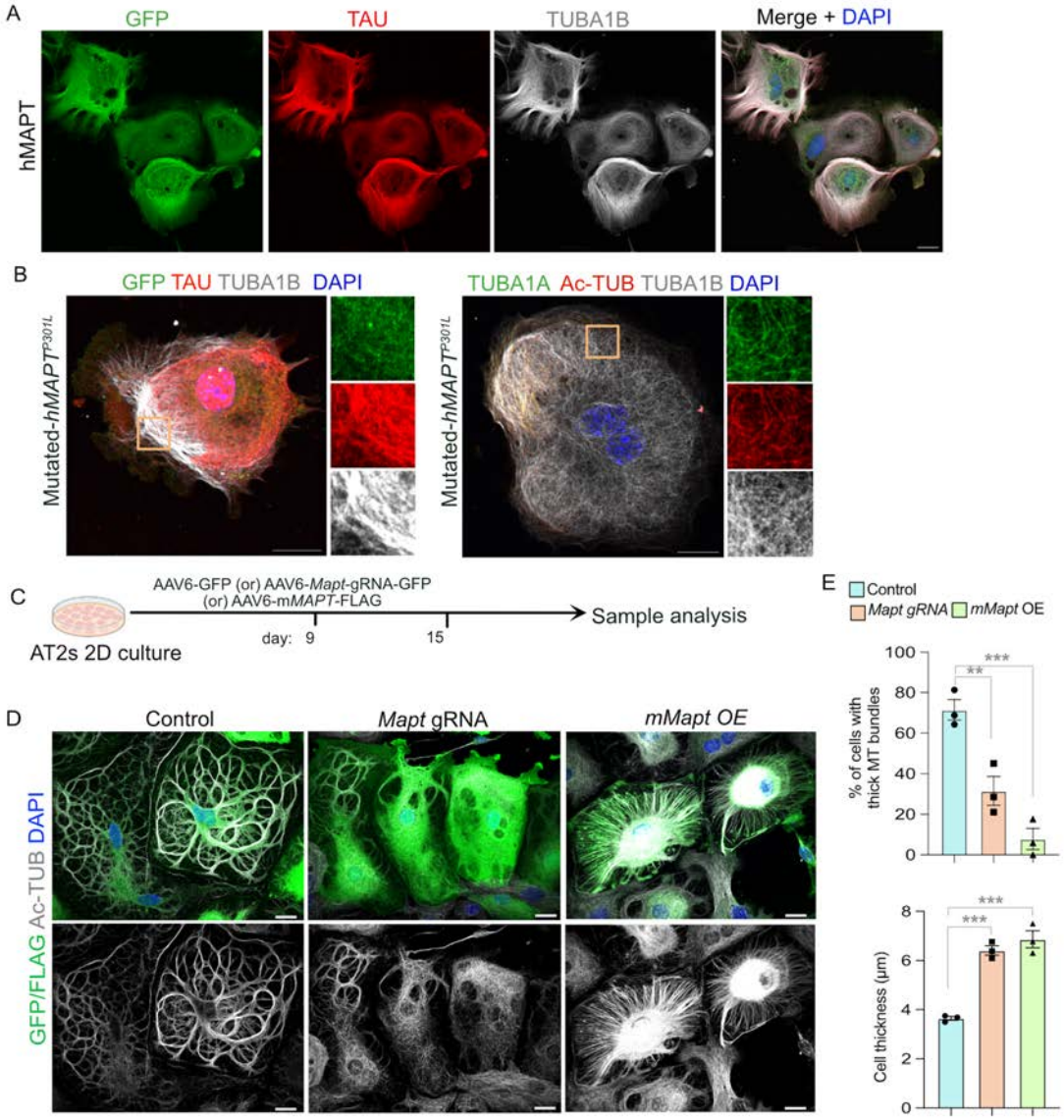

Supplemental Figure 5. Ectopic expression of WT hMAPT or mutated hMAPT^{P301L} and *Mapt-KO* disrupts thick MT-bundle formation. (A) Staining for GFP (green), TAU (red) and TUBA1B (grey) in hMAPT-overexpressed cell (green). Scale bars: 20μm. (B) Staining for GFP (green), TAU (red) and TUBA1B (grey) (left image) and TUBA1A (green), Ac-TUB (red) and TUBA1B (grey) in hMAPT^{P301L} overexpressed cells. DAPI stains nuclei (blue). (C) Experimental workflow for AT2-AT1 differentiation followed by *AAV6-Mapt* gRNA or *AAV6-Mapt-OE* administration and sample collection. (D) Staining for Ac-TUB (grey) in virus infected (green) *Mapt-KO*, *Mapt*-OE, and control cells. (E) Percentage of transduced cells exhibiting thick MT-bundles and quantification of cell thickness. ** p=0.005, *** p<0.001. one-way ANOVA. Data are presented as mean ± s.e.m. n=3 biological replicates.

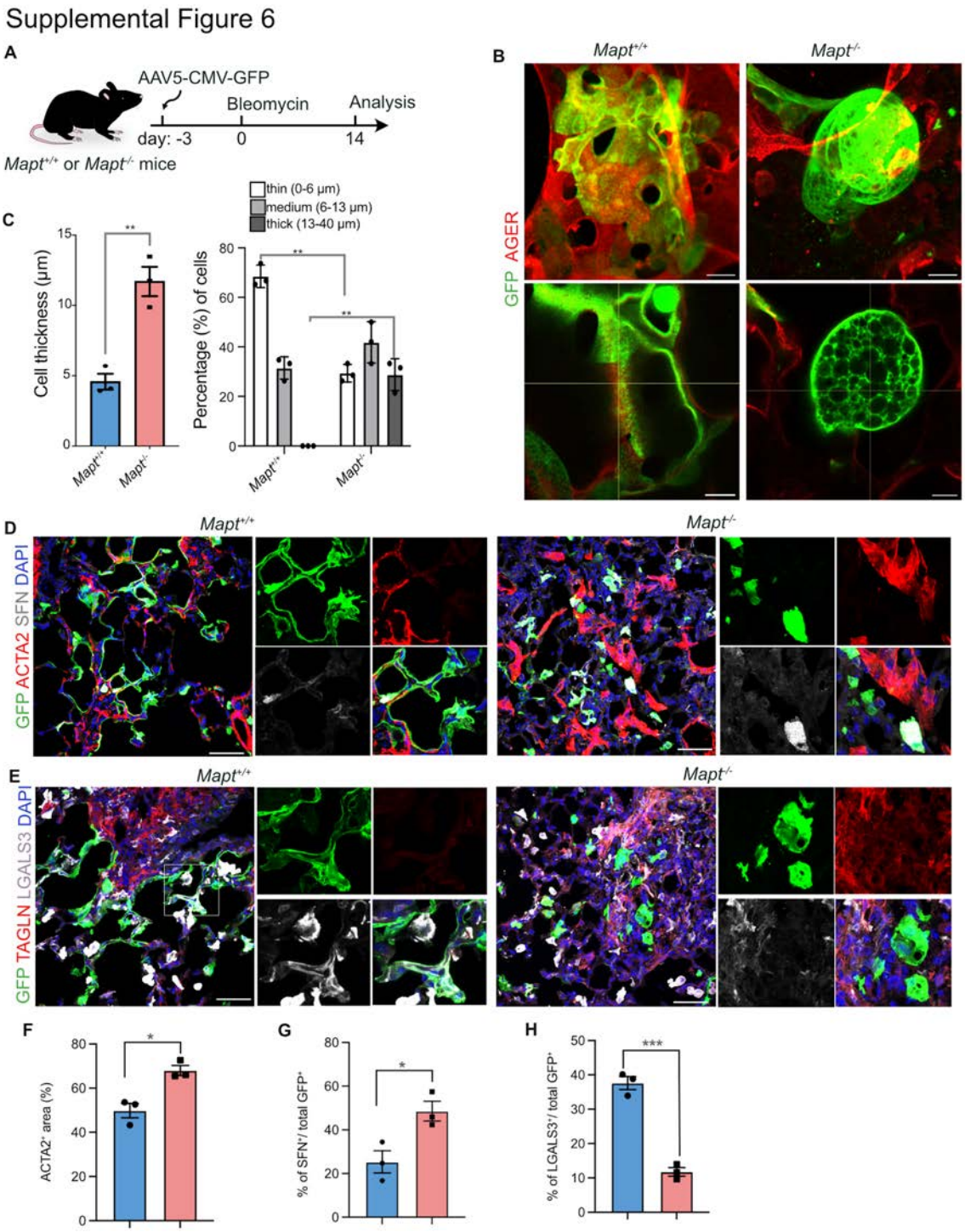

Supplemental Figure 6. *Mapt* deficient AT2s exhibit balloon-like cell morphology in response to bleomycin-induced lung injury. (A) Schematic of experimental workflow for AT2 labelling using AAV5-GFP followed by bleomycin injury for lung sample collection from controls and *Mapt-/-* mice. (B) Staining for GFP (green) and AGER (red) in controls and *Mapt-/-* mice after bleomycin injury. Scale bars: 20µm. (C) Quantification on cell thickness and the distribution of

GFP$^+$ cells with different thickness in wild type control and *Mapt-/-* lungs after bleomycin injury. ***p<0.005*, unpaired two-tailed t-test. (D) Staining for GFP (green), ACTA2 (red) and SFN (grey) in controls and *Mapt-/-* mice after bleomycin injury. Scale bars: 50μm. (E) Staining for GFP (green), TAGLN (red), and LGALS3 (grey) in controls and *Mapt*-deleted AT2s after bleomycin injury. Scale bars: 50μm. DAPI stains nuclei (blue). (F) Quantification of ACTA2$^+$ area of the bleomycin injured lungs. *$p<0.05$ unpaired t-test. (G) Quantification of SFN$^+$ cells within all GFP$^+$ cells in bleomycin injured lungs. *$p<0.05$, unpaired t-test. (H) Quantification of LGALS3$^+$ cells within all GFP$^+$ cells in bleomycin injured lungs. ***$p<0.001$, unpaired t-test. Data in C, F, G and H are presented as mean ± s.e.m. n=3 biological replicates.

Supplemental Figure 7

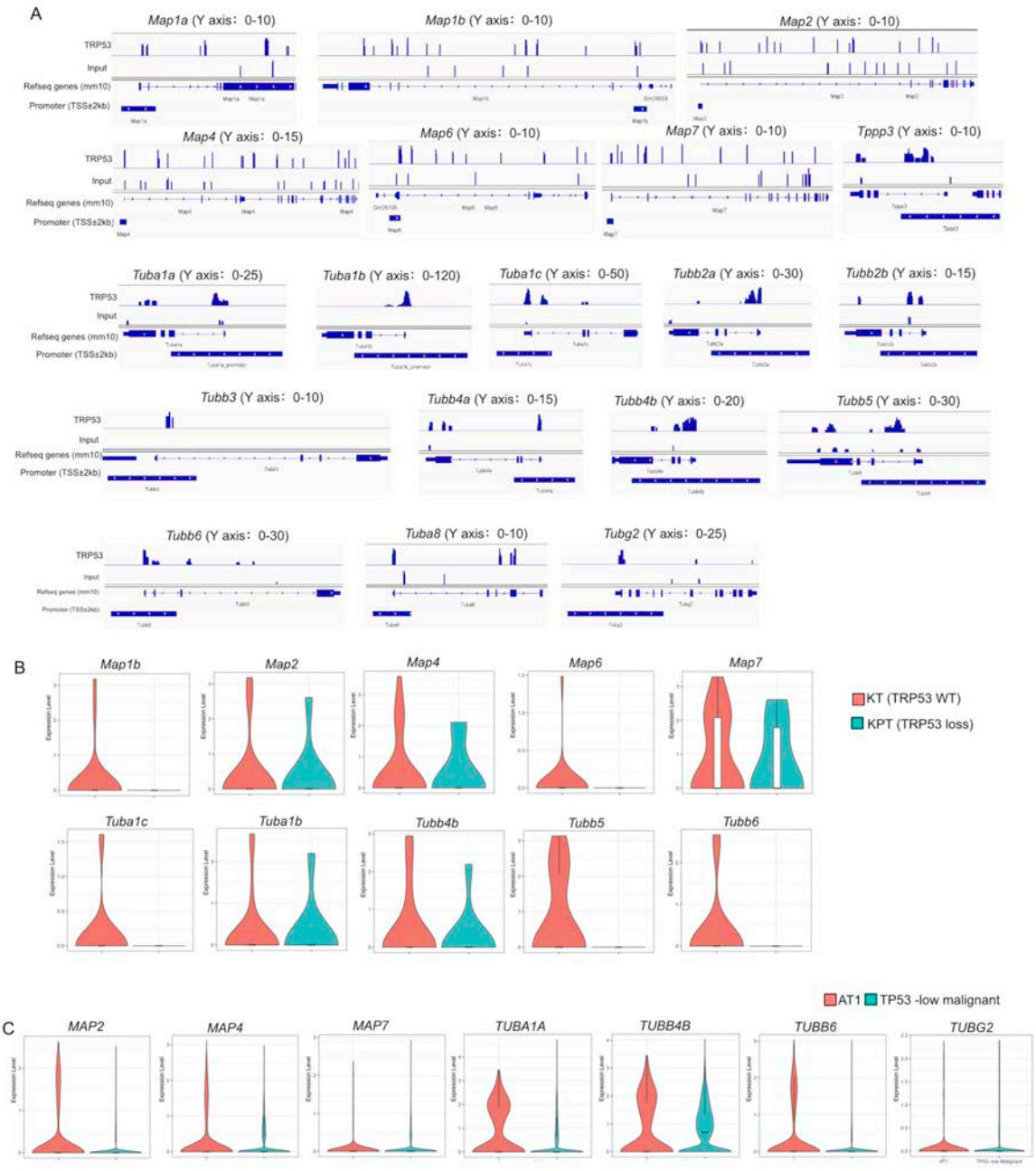

Supplemental Figure 7. **TP53 directly binds on promoters of distinct microtubule related genes and regulates their expression.** (A) IGV tracks show significant enrichment for TRP53 binding in genomic loci corresponding to indicated microtubule associated genes. (B) Violin plots showing the expression of indicated genes in AGER-positive AT1-like cells from KT (TRP53 WT) and KPT (TRP53 loss) lungs in the Kras-driven mouse lung cancer. (C) Violin plots showing the expression of indicated gens in AT1s and TP53-low malignant epithelial cells from the human lung adenocarcinoma. All plots display log-normalized RNA expression values.

Supplemental Figure 8

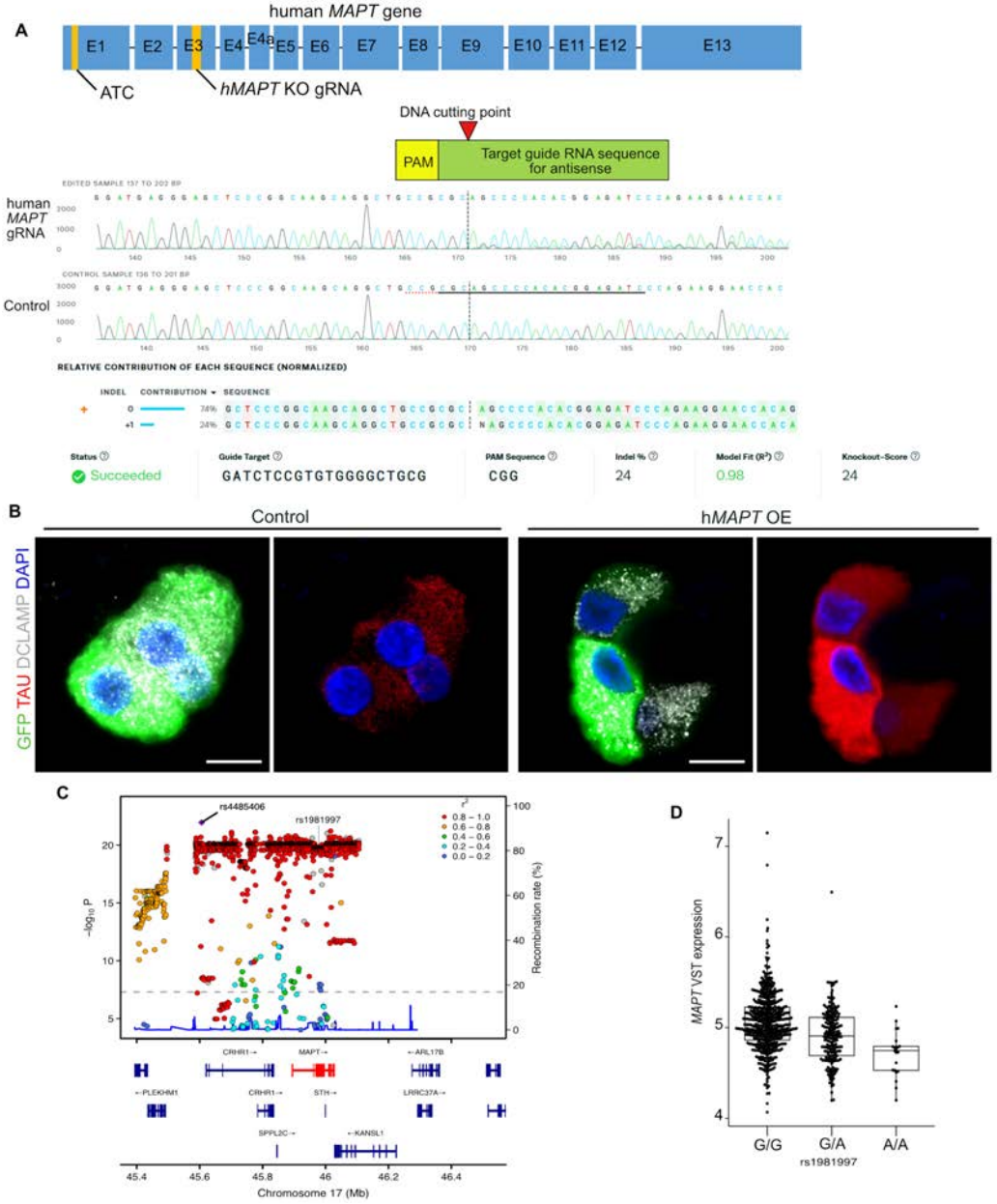

Supplemental Figure 8. Characterization of human *MAPT* gRNA efficiency, MAPT gain of function and GWAS analyses. (A) Representative Sanger chromatograms and indel efficiency analysis in controls and h*Mapt gRNA* edited cells. (B) Staining for GFP (green), TAU (red) and an AT2 marker-DC-LAMP (grey), on *MAPT*-overexpressed and control hAT2s. Scale bars: 20μm. DAPI stains nuclei (blue). (C) *MAPT* cis-eQTL Locus Zoom plot of nasal airway brushing data from the GALA cohort, showing a strong LD block marking the *MAPT* eQTL. Linkage disequilibrium is centered on the lead eQTL SNP, rs4485406. (D) *MAPT* expression in nasal brushings stratified by genotype at the IPF risk variant, rs1981997.

Videos Legends

Video 1. Morphological changes in differentiating alveolar epithelial cells. Bright field and epifluorescence (*tdTomato*) showing differentiating alveolar epithelial cells.

Video 2. Tubulin dynamic in transitional epithelial states. Time-lapse images illustrating tubulin dynamics (EB1-EGFP) and orientation in cells cultured for 7-days.

Video 3. Tubulin dynamic in AT1s. Time-lapse images illustrating tubulin dynamics and orientation in cells cultured for 14-days.

Video 4. Tubulin dynamic in *Trp53*-KO alveolar epithelial cells cultured for 7-days. Time-lapse images illustrating tubulin dynamics and orientation in cells cultured for 7-days.

Video 5. Loss of *Trp53* in alveolar epithelial cells leads to disrupted tubulin dynamics in *ex vivo* day-14 cultures. Time-lapse images illustrating tubulin dynamics and orientation in cells cultured for 14-days.